

Single-particle dynamics in the vicinity of the Mott-Hubbard metal-to-insulator transition

Michał Karski*

Institut für Angewandte Physik der Universität Bonn, Wegelerstrasse 8, 53115 Bonn, Germany

Carsten Raas[†] and Götz S. Uhrig[‡]

Lehrstuhl für Theoretische Physik I, Otto-Hahn-Straße 4, Universität Dortmund, D-44221 Dortmund, Germany

(Received 11 October 2007; published 15 February 2008)

The single-particle dynamics close to a metal-to-insulator transition induced by strong repulsive interaction between the electrons is investigated. The system is described by a half-filled Hubbard model which is treated by dynamic mean-field theory evaluated by high-resolution dynamic density-matrix renormalization. We provide theoretical spectra with momentum resolution which facilitate the comparison to photoelectron spectroscopy.

DOI: [10.1103/PhysRevB.77.075116](https://doi.org/10.1103/PhysRevB.77.075116)

PACS number(s): 71.30.+h, 75.40.Gb, 71.27.+a, 71.28.+d

I. INTRODUCTION

Strongly correlated systems are notoriously difficult to understand. In particular, this is true when parameter regions are considered where the system changes its behavior qualitatively, for instance, where new excitations emerge. This is precisely the situation around the metal-to-insulator transition of electrons which repel each other strongly on a tight-binding lattice due to the Coulomb interaction.

We consider a half-filled lattice with one electron per site on average. For strong on-site repulsion, it is energetically forbidden that two electrons occupy the same site. Because there is one electron per site on average this implies that there is precisely one electron per site. No electron can move so that the system is insulating. The remaining degree of freedom is the orientation of the electron spins. This freedom gives rise to collective magnetic excitations, for instance, spin waves.

For weak interaction, on the other hand, the system is a metal in the sense of a Fermi liquid. This is true if we neglect ordering phenomena, i.e., we focus on the paramagnetic phase. Hence this system is dominated by the quasiparticle excitations. No collective modes play a major role.

In the vicinity of the metal-to-insulator transition the Fermi liquid must change such that precursors of the collective magnetic excitations of the insulator emerge. Vice versa, the collective excitations in the insulator must acquire finite lifetimes so that they broaden considerably in the corresponding spectra if we pass in the insulating regime toward the metallic one. Such behavior can be measured by inelastic neutron scattering, for example.

Hence it is of particular interest to understand the dynamics of the important excitations in the vicinity of an interaction induced metal-to-insulator transition. In the present work, we focus on the single-particle excitations, which means we investigate the single-particle propagation. The investigation is done in the framework of the dynamic mean-field theory (DMFT) which maps the lattice model to an effective single-site problem with a self-consistency condition.¹⁻⁴ The single site is coupled to a bath of noninteracting fermions which can be represented as a semi-infinite chain.

The semi-infinite chain and its head where the interaction takes place can be tackled numerically by algorithms for

one-dimensional systems. We will use density-matrix renormalization for this purpose.^{5,6} Since the dynamic properties have to be determined we use the dynamic density-matrix renormalization with correction vector.^{7,8} Thereby, we dispose of a numerical means which can resolve spectral properties not only at low energies but also at high energies.⁹ This makes it possible to determine sharp spectral features away from the Fermi energy also quantitatively.¹⁰

The main aim of the present paper is to provide comprehensive spectral data in the above mentioned theoretical framework. In particular, we present momentum-resolved single-particle spectral densities in the insulating and in the metallic regime.

In Sec. I A, we will present the model under investigation, i.e., the half-filled one-band Hubbard model with semielliptic density of states (Bethe lattice) at zero temperature. Next, in Sec. II, we will discuss the method. We use the DMFT (Sec. II A) which maps the problem to an effective single-impurity Anderson model (SIAM) (Sec. II B) with a self-consistency condition. The SIAM is treated numerically by a dynamic density-matrix renormalization group (D-DMRG) impurity solver (Sec. II C). The results of this approach are presented in Sec. III, with the spectral properties in the paramagnetic *insulating phase* (Sec. III A) and the paramagnetic *metallic phase* (Sec. III B). The results reveal insights in the nature of the Mott-Hubbard metal-to-insulator transition and provide a numerical proof for previous investigations which were based on the hypothesis of the *separation of energy scales*. Finally, a summary will be given in Sec. IV.

A. Model

We use the generic model for strongly correlated systems in solids, namely, the Hubbard model.¹¹⁻¹³ It is given by the Hamiltonian

$$\mathcal{H} = U \sum_i \left(n_{i,\uparrow} - \frac{1}{2} \right) \left(n_{i,\downarrow} - \frac{1}{2} \right) - t \sum_{\langle i,j \rangle, \sigma} c_{i,\sigma}^\dagger c_{j,\sigma}, \quad (1)$$

where i and j denote sites on a lattice with $\langle i,j \rangle$ being nearest neighbors, $\sigma \in \{\uparrow, \downarrow\}$ the spin, $c_{i,\sigma}^{(\dagger)}$ the electron annihilation (creation) operator, and $n_{i,\sigma}$ their occupation operator. This

model contains the basic ingredients of the problem, i.e., a local repulsive interaction and a kinetic energy consisting of hopping from site to site. The interaction is diagonal in real space and hence tends to make the eigenstates local in real space. The kinetic energy is diagonal in momentum space and hence tends to make the eigenstates local in momentum space implying extended states in real space. So the interaction favors an insulating phase whereas the kinetic energy favors a conducting, metallic phase. They are the antagonists and depending on their relative strength the system is metallic or insulating.

The transition between these two phases has been a long-standing issue. By now, evidence emerges that the transition is continuous at zero temperature^{10,14,15} whereas it is of first order at any finite temperature.¹⁶ The continuous transition at zero temperature is peculiar. It cannot be seen as an ordinary second-order transition. It should rather be seen as a marginal first-order transition with zero hysteresis. At zero temperature, the free energy is continuously differentiable at the transition because the ground-state energy is continuously differentiable. The residual entropy jumps even at zero temperature because the ground state of the metal is the nondegenerate Fermi sea. The insulator, however, is governed by the spin degrees of freedom. Since we do not consider any long-range order they remain free down to zero energy. The freedom to choose the spin locally \uparrow or \downarrow in the paramagnetic insulating phase implies a finite residual entropy of $\ln 2$ per site. However, at zero temperature, the discontinuous entropy does not imply jumps in the other thermodynamic quantities.

II. METHOD

In this section we present the details of the methods that we used to tackle the model and to compute the desired single-particle dynamics. The key points are the dynamic mean-field theory, the single-impurity Anderson model, and the dynamic density-matrix renormalization.

A. Dynamic mean-field theory

The basic idea of the dynamic mean-field theory is to consider the lattice problem under study in the limit of infinite coordination number $z \rightarrow \infty$. This means that the lattice is generalized in a way that z is a tunable parameter. Very often, this is realized by considering related lattices in d -dimensional space. Then $z \propto d$ and the desired limit is the limit of infinite dimensions.

The limit $z \rightarrow \infty$ is well defined only for a particular scaling of the matrix elements in the Hamiltonian (1) which link different sites. In particular, the hopping to the nearest neighbors must be scaled like $1/\sqrt{z}$.^{1,2} Then the single-particle propagator G_{ij} between site j and site i scales like

$$G_{ij} \propto z^{-\|i-j\|/2}, \quad (2)$$

where we use $\|i-j\|$ for the taxi cab metric. This metric counts how many hopping processes are at least necessary to go from j to i .

Considering the standard diagrammatic expansion in powers of the interaction one realizes that the scaling (2) implies

that many diagrams vanish for $z \rightarrow \infty$. Only those which are either completely local or which are sufficiently numerous lead to nonvanishing contributions. Closer inspection shows that only those dressed skeleton diagrams lead to nonvanishing contributions which are completely *local*.^{1,2} This is called the collapse of the diagrams because only a single site occurs. For the proper self-energy Σ this implies that it is local; only Σ_{ii} needs to be considered.

In spite of the very substantial reduction of the number of relevant diagrams their summation is not directly possible. Hence the dynamic mean-field theory requires an additional element. This is the observation that the *same* local dressed skeleton diagrams occur in the treatment of a SIAM where the interaction takes place at the impurity which is coupled to a fermionic bath.^{3,4,17} Hence, the *same* self-energy is obtained *if* the local dressed propagators are the same. Let us use capital letters for the local dressed propagator $G := G_{ii}$ and for the local self-energy $\Sigma := \Sigma_{ii}$ in the lattice model in DMFT. We use small letters for the local dressed propagator g and the self-energy σ at the impurity of the effective single-site problem. Then the above statement reads

$$\Sigma(\omega) = \sigma(\omega) \quad (3a)$$

if

$$G(\omega) = g(\omega) \quad (3b)$$

holds. Note that this does *not* imply that $G^0 = g^0$ where we use the superscript ⁰ for the bare, undressed propagators.

For completeness, we mention that the self-consistency equations (3a) and (3b), which we derived from the expansion in dressed skeleton diagrams, can also be obtained from the action by the so-called cavity argument.¹⁸ A derivation in the strong coupling limit is given in Ref. 18. An elegant derivation of the DMFT including the possibility to generalize from single site to cluster systems has been found by Potthoff¹⁶ in the framework of variational self-energy functionals.

Equations (3a) and (3b) face us with the problem that we do not know the bare propagator of the SIAM. This amounts up to a generic self-consistency problem where we first have to guess a g^0 and then we can verify whether the conditions (3a) and (3b) are fulfilled.

Following this roadmap, two more fundamental relations are needed, namely, the Dyson equations of the lattice problem and of the SIAM. The local self-energy Σ_{ii} acts on every site equally since we consider the uniform, paramagnetic phase. For this reason we could omit the subscript and pass on to Σ . This spatially constant energy acts like a global energy shift so that it can be accounted for by

$$G(\omega) = G^0(\omega - \Sigma(\omega)), \quad (4)$$

which is the Dyson equation for the lattice problem.

In the single-site problem, the self-energy $\sigma(\omega)$ acts only on the impurity site. The bare propagator from the impurity site to the impurity site is $g^0(\omega)$ so that the Dyson equation is given by the geometric series

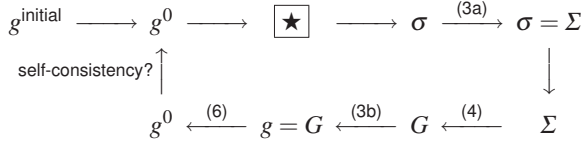


FIG. 1. Schematic representation of the iterative self-consistency cycle for an arbitrary lattice. In the step marked with ★ the dynamics of an effective single-impurity Anderson model is calculated by a D-DMRG impurity solver.

$$g(\omega) = g^0 + g^0 \sigma g^0 + g^0 \sigma g^0 \sigma g^0 + \dots + g^0 (\sigma g^0)^n + \dots$$

$$= \frac{g^0(\omega)}{1 - g^0(\omega) \sigma(\omega)}. \quad (5)$$

This relation can also be written as

$$1/g = 1/g^0 - \sigma. \quad (6)$$

The above equations are used to set up an iteration cycle to find a self-consistent solution. It is illustrated in Fig. 1. Starting in the upper left corner, an initial guess is used to define the SIAM which is then solved by an impurity solver providing σ . Then σ is used as lattice self-energy Σ providing via the lattice Dyson equation (4) the dressed propagator for the lattice. By the condition (3b) the dressed propagator of the SIAM is known which in turn yields via Eq. (6) its bare counterpart so that we are at the beginning of the cycle again. If the bare propagator is close enough to the previous assumption, the iterations are stopped. Details of the precise meaning of how close is close enough are given in Sec. II C 4.

The above sketched cycle can be used for any lattice, i.e., for any G^0 . For a particular G^0 with semielliptic spectral density of states (DOS) $\rho^0(\omega) := -(1/\pi) \text{Im} G^0(\omega)$

$$\rho^0(\omega) = \frac{2}{\pi D^2} \sqrt{D^2 - \omega^2}, \quad (7)$$

the cycle can be simplified considerably. A semielliptic spectral density $\rho^0(\omega)$ corresponds to the so-called Bethe lattice with infinite branching ratio.¹⁹ Note that we do not use any other feature from the Bethe lattice other than Eq. (7). Hence our calculation can be viewed as treating a translationally invariant lattice with a semielliptic DOS. This is a good starting point for generic spectral densities since it is bounded and it possesses square-root singularities at the band edges such as three-dimensional densities of states have. Otherwise it is featureless.

The key feature of G^0 with semielliptic $\rho^0(\omega)$ is its particularly simple continued fraction representation with constant coefficients

$$G^0(\omega) = \frac{1}{\omega - \frac{D^2/4}{\omega - \frac{D^2/4}{\omega - \dots}}}. \quad (8)$$

In order to use this fact for simplification we write the bare propagator of the SIAM with the help of the so-called hybridization function $\Gamma(\omega)$ as

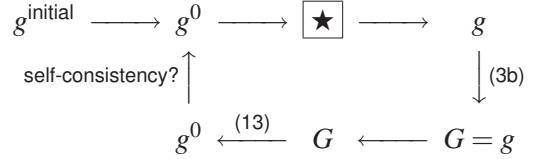


FIG. 2. Schematic representation of the iterative self-consistency cycle for semielliptic density of states (DOS) with nearest-neighbor hopping. The step ★ stands for the D-DMRG impurity solver.

$$g^0(\omega) = \frac{1}{\omega - \Gamma(\omega)}, \quad (9)$$

where the continued fraction of $\Gamma(\omega)$ shall be parametrized like

$$\Gamma(\omega) = \frac{V^2}{\omega - \frac{\gamma_0^2}{\omega - \frac{\gamma_1^2}{\omega - \dots}}}. \quad (10)$$

Then, based on Eqs. (6) and (3a) the dressed propagator of the SIAM reads

$$\frac{1}{g(\omega)} = \omega - \Gamma(\omega) - \Sigma(\omega). \quad (11)$$

By Eqs. (4) and (8) the dressed propagator of the lattice can be expressed to be

$$\frac{1}{G(\omega)} = \omega - \Sigma(\omega) - \frac{D^2/4}{\omega - \Sigma - \frac{D^2/4}{\omega - \Sigma - \frac{D^2/4}{\omega - \Sigma \dots}}}$$

$$= \omega - \Sigma(\omega) - (D^2/4)G(\omega), \quad (12)$$

where we exploited that the continued fraction does not change when it is evaluated at a deeper level because its coefficients are constant.

Based on the self-consistency condition (3b) we set Eqs. (11) and (12) equal and obtain the simpler self-consistency condition

$$\Gamma(\omega) = \frac{D^2}{4} G(\omega). \quad (13)$$

This equation is more easily used because it provides a direct way to compute the hybridization function $\Gamma(\omega)$ of the next iteration of the SIAM from the dressed lattice propagator G . No explicit computation of intermediate self-energies is needed which can be severely hampered by numerical errors, see below. A first conclusion which can be drawn from Eq. (13) is that $V=D/2$.

The resulting cycle is given graphically in Fig. 2. This form of the iteration cycle is used in the present work.

B. Single-impurity Anderson model

There are various ways to set up the effective single-impurity problem because the precise topology of the fermi-

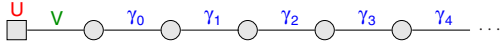


FIG. 3. (Color online) Sketch of the semi-infinite chain which is used as topology for the single-impurity Anderson model.

onic bath, to which the impurity couples, does not matter. As we have seen in the equations above we are only concerned with the local quantities on the impurity. Hence the only relevant property of the fermionic bath is the bare propagator g^0 or the hybridization function Γ , respectively.

Because we aim at the application of density-matrix renormalization, which has been developed for one-dimensional systems, in particular, we favor the representation of the bath as semi-infinite chain, see Fig. 3. This is no restriction since mathematically any hybridization function which has a non-negative spectral density can be represented as continued fraction²⁰ as given in Eq. (10). By complete induction it is straightforward to see that the choice of the hopping elements shown in Fig. 3 implies Eq. (10).

The Hamiltonian of the SIAM represented as linear chain reads²¹

$$\mathcal{H} = U \left(n_{d,\downarrow} - \frac{1}{2} \right) \left(n_{d,\uparrow} - \frac{1}{2} \right) + V \sum_{\sigma} (d_{\sigma}^{\dagger} c_{0,\sigma} + \text{H.c.}) + \sum_{n=0,\sigma}^{\infty} \gamma_n (c_{n,\sigma}^{\dagger} c_{n+1,\sigma} + \text{H.c.}). \quad (14)$$

The correlations stem from the density-density coupling on the impurity site (d^{\dagger} operators) at the head of a semi-infinite chain of free fermions (c^{\dagger} operators). For comprehensive information on the physics of single-impurity Anderson models the reader is referred to Ref. 21.

The determination of the local propagator $g(\omega)$ in the effective SIAM (14) for a given hybridization function $\Gamma(\omega)$ is the most difficult part in the self-consistency cycles (cf. Figs. 1 and 2). The necessary tool is called the *impurity solver*.

The dynamics one has to compute is the dynamics of the fermionic single-particle propagator of the impurity electron. Aiming at the properties at $T=0$ it reads

$$g(\omega + i\eta) = \langle 0 | d_{\sigma} \frac{1}{\omega + i\eta - (\mathcal{H} - E_0)} d_{\sigma}^{\dagger} | 0 \rangle + \langle 0 | d_{\sigma}^{\dagger} \frac{1}{\omega + i\eta + (\mathcal{H} - E_0)} d_{\sigma} | 0 \rangle. \quad (15)$$

Here the ground state is denoted by $|0\rangle$ and its energy by E_0 . Since we aim at the paramagnetic phase the propagator has no dependence on the spin index σ and we do not denote it. The frequencies ω and η are real. The standard retarded propagator is retrieved for $\eta \rightarrow 0+$

$$g_R(\omega) = \lim_{\eta \rightarrow 0+} g(\omega + i\eta). \quad (16)$$

The wanted quantity is the spectral density $\rho(\omega) := -\pi^{-1} \text{Im } g_R(\omega)$. If necessary the real part of $g_R(\omega)$ can be obtained from $\rho(\omega)$ by the Kramers-Kronig relation

$$\text{Re } g_R(\omega) = \mathcal{P} \int_{-\infty}^{\infty} \frac{\rho(\omega')}{\omega - \omega'} d\omega', \quad (17)$$

where \mathcal{P} denotes the principal value.

C. Dynamic density-matrix renormalization

1. Algorithm

Because there are essentially no analytic approaches available which solve the general SIAM, reliable numerical approaches for dynamic correlations are very important. Our choice is the dynamic density-matrix renormalization which is an excellent tool for calculations for open one-dimensional systems at zero temperature.

To obtain $g(\omega)$ for a given $\Gamma(\omega)$ we use a combination of the D-DMRG^{7,8,22} and the least-bias deconvolution algorithm.²³ The D-DMRG is the generalization of the standard DMRG^{5,6} for the calculation of dynamic quantities. A key advantage over other $T=0$ approaches such as the numerical renormalization group is that the resolution can be high not only at low energies but also at high energies.⁹ We implemented the D-DMRG in a correction vector (CV) scheme^{7,8,24} with optimized direct matrix inversion; for details, see Refs. 9 and 25.

The actual calculations are not performed for the fermionic representation (14) but for a spin representation involving two semi-infinite spin chains which are coupled at their heads. This spin representation replaces each fermionic level with states empty and occupied by the two spin states \uparrow and \downarrow . The change of basis between both representations is accomplished by two Jordan-Wigner transformations, one for the \uparrow electrons and one for the \downarrow electrons, see Ref. 9. The resolvents appearing in Eq. (15) are expressed as resolvents of the equivalent spin system involving spin flips at the head of the chains. The advantage for the DMRG approach is that in the spin chain description each site carries only a two-dimensional Hilbert space instead of a four-dimensional one.

The correction vector D-DMRG provides data points at given frequencies $\omega = \omega_i$ for finite values of $\eta = \eta_i$

$$g_i := -\frac{1}{\pi} \text{Im } g(\omega_i + i\eta_i) \quad (18a)$$

$$= \rho(\omega) \otimes L_{\eta_i}(\omega) |_{\omega=\omega_i} \quad (18b)$$

$$= \frac{1}{\pi} \int_{-\infty}^{\infty} \frac{\eta_i \rho(\omega) d\omega}{(\omega - \omega_i)^2 + \eta_i^2}, \quad (18c)$$

where $\otimes L_{\eta_i}(\omega)$ stands for the convolution with a Lorentzian of width η_i . No data can be obtained directly at $\eta=0$ since the inversion of the Hamiltonian is singular and cannot be achieved numerically in a stable way. Furthermore, we cannot numerically treat an infinite chain but only a finite one.

Henceforth, we will call data $\{g_i\}$ *raw* data because it is obtained at finite values of η_i . Apart from the constraint from matrix inversion, a sufficiently large broadening η_i is used in order to calculate continuous spectral densities resembling the spectral densities in the thermodynamic limit. The finite-

size effects are washed out. In a second step, we aim at retrieving the unbroadened spectral density $\rho(\omega)$ as well as possible.

We use the D-DMRG raw data calculated for a finite set of frequencies ω_i with nonzero broadenings η_i as input of a deconvolution scheme to extract the information on the spectral density $\rho(\omega)$, i.e., the relevant dynamic properties of the infinite system. The deconvolution scheme of our choice is the least-bias (LB) approach²³ which belongs to the class of maximum entropy methods.²⁶ The combination of D-DMRG and LB deconvolution has already proven itself in the investigation of the high-energy dynamics of the SIAM by providing a well-controlled resolution for all energies.^{23,25} By construction, the LB ansatz yields a positive and continuous result for the density of states $\rho(\omega)$ (DOS). The positiveness assures the causality of the solution, which is necessary for calculating the continued fraction, see Appendix A, whereby the DMFT self-consistency cycle is closed. By using the LB deconvolution we avoid any kind of arbitrariness introduced by the choice of a discretization mesh.

Of course, the direct computation of a continuous density from data obtained for a finite system involves an approximation. In practice, one must pay attention whether the system size and the broadening considered make it possible to deduce continuous densities, see also below.

Nishimoto *et al.*^{27,28} advocated a different approach which has been baptized “fixed-energy” DMFT where the problem of deducing *densities* is circumvented by discretizing the continuous frequency in a number of bins. For these bins the spectral *weights* are computed. On the one hand, spectral weights are better behaved for finite system sizes. However, on the other hand, the DMFT self-consistency holds only for the continuous quantities in Eqs. (3a) and (3b). So any extension to discrete quantities introduces some ambiguity.²⁹ Balancing these two contrary aspects we have chosen to work with the continuous spectral densities as obtained from the LB ansatz.

In the framework of the D-DMRG Jeckelmann has formulated a variational principle for the wanted dynamic correlation.³⁰ A certain functional is minimum for the correct dynamic correlation. Its value yields the g_i as defined in Eq. (18a). Due to the minimum principle this approach is rather robust. Its main advantage is that even if the numerical dynamic correlation possesses an error δ the values g_i will be exact up to quadratic order δ^2 . From the algorithmic viewpoint the minimization required for Jeckelmann’s approach is more demanding than the matrix inversion in the D-DMRG with correction vector. Hence we stick to an optimized matrix inversion.^{9,25} In our opinion, the optimum strategy is to search for the best correction vector by optimized matrix inversion and then to use the variational functional for the evaluation of the g_i .

2. Deconvolution and finite-size effects

The choice of the η_i for a given set of ω_i is restricted by the considered chain length L . If the η_i are chosen too small, the extracted spectral properties reveal too strong finite-size effects. If the η_i are chosen too large, essential features in the spectral properties cannot be resolved properly and therefore

remain smeared out, even after the deconvolution. Thus, the optimum value of each η_i has to be chosen with care depending on the width of the features which have to be resolved. In our approach the optimum choice is characterized by

$$\eta_i \approx \Delta\omega_i \gg W^*/L, \quad (19)$$

where $\Delta\omega_i$ denotes the distance between two neighboring frequencies and W^* is the bandwidth. The approximate equality between η_i and $\Delta\omega_i$ reflects the fact that it is not reasonable to numerically measure the spectral density which is broadened by η_i at frequencies much closer than η_i . This does not lead to an increase of relevant information about the underlying unbroadened spectral density. In contrast, it might happen that small errors lead to inconsistencies of the too closely positioned data points so that the subsequent deconvolution leads to strongly oscillatory results.²³

The inequality $\Delta\omega_i \gg W^*/L$ in Eq. (19) results from the approximation of the infinite system under study by a finite system. If the points ω_i , at which the broadened spectral density is measured numerically, were too closely spaced the finite-size effects would be discernible. Hence the raw data $\{g_i\}$ could not be processed as if it resulted from a continuous spectral density.

Finally, we point out, that apart from the resolution aspect, the choice of η_i influences the stability and the performance of the correction vector D-DMRG. For very small values of η_i the matrix inversions are numerically very demanding and time consuming.

3. Continuous fraction

The LB algorithm and the Kramers-Kronig transformation allow us to extract the full unbroadened Green function $g(\omega)$ to good accuracy from the raw D-DMRG data for an arbitrary ω . Thus we can have an arbitrary number of supporting points for further numerical calculations. The hopping elements γ_n of the effective SIAM (14) for the next iteration in the self-consistency cycle are calculated recursively by a continued fraction expansion.^{20,31} Note that even tiny regions of small negative spectral density spoil the continued fraction expansion completely. The details of the calculation of the continued fraction are given in Appendix A.

4. Numerical criteria for self-consistency

We have realized the iterative cycle shown in Fig. 2. Since we perform the calculation of the spectral densities numerically, including an advanced deconvolution scheme, the calculation of two *identical* spectral densities within the iterative self-consistency cycle is not possible by principle. Consequently, a certain error tolerance has to be included to the termination conditions.

A solution within our DMFT self-consistency cycle is understood as self-consistent, if at least the following conditions are fulfilled.

(1) Two deconvolved spectral densities calculated consecutively within the self-consistency cycle obey for all ω ,

$$|\rho^{(i)}(\omega) - \rho^{(i+1)}(\omega)| < \varepsilon, \quad (20)$$

where $\varepsilon = 4 \times 10^{-3}/D$ for the metallic and $\varepsilon = 10^{-3}/D$ for the insulating solutions.

(2) The average double occupancy and the ground-state energy per lattice site calculated in succession within the self-consistency cycle are stable. That means that they differ by less than $10^{-2}\%$.

For the insulating solutions, we additionally require that the *static* single-particle gaps calculated consecutively by means of the standard DMRG algorithm differ by less than 1%. The higher value of ε for the metallic solutions has to be chosen because the metallic spectral densities display a high complexity including many sharp features. In contrast, the spectral densities of the insulating solutions are rather featureless and thus converge more easily.

We stress that the upper conditions are the minimum requirement and that most of our solutions surpass them considerably. However, we observed that it is sufficient to terminate the self-consistency cycle once the upper conditions are fulfilled. The physical quantities obtained from the continued fractions computed in two consecutive iterations are almost identical. Further iterations yield no further improvement. Moreover, we have confirmed that our final continued fraction coefficients do not display persistent trends of change if iterated further. They rather display very small oscillations around the results which we consider to be converged.

5. Numerical stability of the metallic and the insulating solution

There is a parameter region in the Hubbard model in infinite dimensions with an interaction U between U_{c1} and U_{c2} where both solutions are locally stable. In a numerical treatment of this situation one has to introduce a bias, preferably minute, which selects the solution we want to find.

This can be done elegantly by exploiting an even-odd effect. If we consider only the impurity site, the bare DOS $\rho^0(\omega)$ consists of a single δ peak at $\omega=0$. Any arbitrary finite repulsion $U>0$ splits this peak into two so that a gap $\Delta=U/2$ occurs. The corresponding self-energy has a pole at $\omega=0$ which is necessary to induce the splitting of the central peak. Hence this self-energy is the self-energy of an insulator.

Any SIAM with an odd number of fermionic sites (one impurity site and an even number of bath sites) has a bare DOS $\rho^0(\omega)$ with a δ peak at $\omega=0$. This lowest-energy level can be occupied or unoccupied without changing the ground-state energy. A finite repulsive interaction will lift this degeneracy partly and split the central δ peak into two and a gap occurs. Of course, if the levels in the bare system lie very close to each other the occurring gap can be very small. However, in any case, the solution resembles an insulating one. We conclude that the use of a SIAM with an odd number of sites implies a small bias toward an insulating solution. Obviously, the relative bias is of the order of the inverse system size $1/L$.

Conversely, considering a SIAM with an even number of sites amounts up to a small bias toward a self-energy belonging to a metallic phase. The imaginary part of Σ at $\omega=0$ is zero.

While the metallic solutions correspond to the Fermi sea as unique ground state the paramagnetic insulating solution implies a macroscopically large degeneracy in the lattice

problem. In the SIAM, the degeneracy is only 2. It stems from the fact that the spin of the impurity is not completely screened by the coupling to the bath because the bath is gapped by Δ . So there is no DOS at low energies and the renormalization of the unscreened moment stops at the lower cut-off Δ . Indeed, we found that the insulating baths show a twofold degenerate ground-state or two almost degenerate low-lying states.

The spin degeneracy in the insulator poses a problem to the numerical treatment. It happens easily that the DMRG algorithm looking for the ground state provides a state with a certain finite magnetization in z direction. If such a solution is used further in the iteration cycle results are produced which do not describe the paramagnetic insulating phase. In order to avoid this problem, we first search for the ground-state $|1\rangle$ with energy E_1 using a standard Lanczos or Davidson algorithm starting from an initial guess $|I_1\rangle$. The degenerate or almost degenerate second state $|2\rangle$ is found from a second run starting from the orthogonal initial guess $|I_2\rangle = |I_1\rangle - \langle 1|I_1\rangle|1\rangle$. With both states we can construct a ground state without magnetization. We use the normalized superposition $|0\rangle = \alpha_1|1\rangle + \alpha_2|2\rangle$ with $1 = |\alpha_1|^2 + |\alpha_2|^2$ where the coefficients are chosen such that

$$\langle 0|d_\sigma d_\sigma^\dagger|0\rangle = \frac{1}{2} \quad (21)$$

for $\sigma = \{\uparrow, \downarrow\}$ which ensures the absence of a magnetization in z direction.

Finally, we note that the treatment of the spectral density in the region of the single-particle gap Δ in the insulating phase requires care. The LB deconvolution scheme does not allow for zero spectral density so that some artifacts need to be removed before the continued fraction expansion can be calculated as explained in Appendix A. The details of the removal of deconvolution artifacts are given in Appendix B.

III. RESULTS

Here we present the results for various spectral densities which we have obtained by the approach described so far. First we focus on the insulating solutions; then we pass on to the metallic solutions. The results are interpreted as well as compared to previous results.

A. Insulator

1. Local spectral densities

The computation of the insulating spectral densities is performed for 121 fermionic sites, including the impurity. Larger system sizes provide identical solutions (not shown). This is related to the relatively low complexity of the insulating solutions which do not display particular features besides the insulating gap.

We calculate the raw D-DMRG data on a grid using mostly $\Delta\omega_i = \eta_i = 0.1D$. Close to the edges of the Hubbard bands we increase the resolution by choosing $\Delta\omega_i = \eta_i = 0.05D$ and partially $0.025D$ or even $\Delta\omega_i = \eta_i = 0.01D$ for $U=2.4D$. This is done to resolve the gap and the band edges

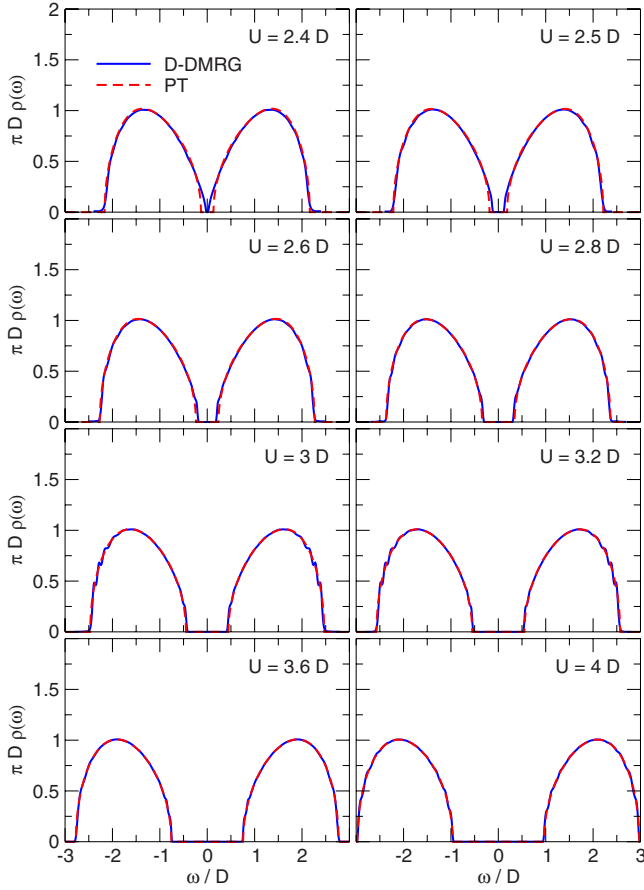


FIG. 4. (Color online) Spectral densities $\rho(\omega)$ in the insulating regime (solid line) calculated with a chain of 121 fermions. The dashed lines (almost coinciding) show the results from strong coupling perturbation theory (Ref. 32).

properly. Note that such a small broadening is useful here, although $\eta_i=0.01D$ does not obey the inequality (19), because it helps us to decide where the spectral density is finite or zero.

The insulating solutions in Fig. 4 clearly show the lower and the upper Hubbard bands each with a bandwidth of nearly $2D$. The bands are separated by a well pronounced gap of 2Δ .⁵⁹ The center of each Hubbard band is located at roughly $\omega = \pm U/2$. The shape of the density in the Hubbard bands in our insulating solutions is essentially smooth and reveals no significant features. They agree very well with the perturbative results by Gebhard *et al.*³² which are based on a strong coupling expansion in $1/U$. Only for very small gaps $\Delta \approx 0.2D$ a noticeable deviation is discernible, see Fig. 5. Clearly, these deviations result from the limited number of terms which are available in the perturbation series.

In Ref. 33 a DMFT calculation based on another DMRG impurity solver, the Lanczos method, showed many substructures in the Hubbard bands. The comparison to our featureless bands leads us to the conclusion that the peaky substructures in Ref. 33 stem from finite-size effects. First, such effects enter because only 45 fermionic sites were considered. Second, the reliable application of the Lanczos impurity solver would require a large number (≈ 100) of target

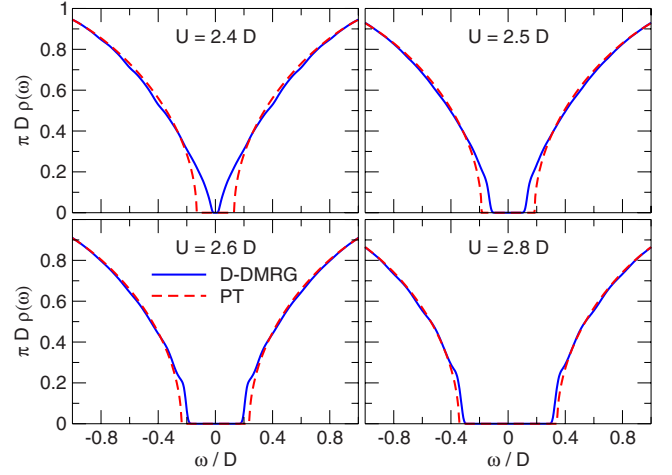


FIG. 5. (Color online) Data from Fig. 4 on a zoomed scale close to the inner band edges.

states which cannot be handled by the DMRG.

The results in Ref. 34 differ from ours only in one important aspect. Nishimoto *et al.* found an upturn of the spectral density $\rho(\omega)$ close to the inner band edge for small gaps which is completely absent in our data. We believe that this difference stems from the different treatment of the spectral density in the gap region, for our approach see Appendix B. In our calculations, the approach of Nishimoto *et al.* to use the extrapolated static gap as a cutoff for the spectral density did not lead to stable self-consistent solutions. On iteration, the spectral density becomes peakier and peakier. The normalization does not hold anymore.

However, we found that a slightly too large gap value tends to produce features similar to the upturns in Ref. 34. Our approach is corroborated further by the excellent agreement between our value of the interaction $U_{c1} = (2.38 \pm 0.02)D$ below which no insulating solution exists and the one obtained by extrapolating the $1/U$ expansion of the ground-state energy. The latter is supported also by quantum Monte Carlo results.^{35,36} In spite of the evidence mentioned above, one may certainly argue in favor of the fixed-energy approach used in Ref. 34 or in favor of the approach used here because both numerical approaches comprise some approximations. For further comparison, see also Sec. III A 2.

The perturbation theory³² implies a square-root behavior at the band edges. The extremely good agreement between the perturbative and the numerical results in Figs. 4 and 5 suggests that a square-root onset is the correct description

$$\rho_{\text{UHB}}(\omega) \propto (\omega - \Delta)^{1/2} \quad (22)$$

at the inner band edges of the upper Hubbard band (UHB).

In order to investigate the behavior of the spectral density quantitatively near the band edges, see Fig. 5, we fit

$$f(\omega) = \Theta(\omega - \Delta)[(\omega - \Delta)^\alpha P_3(\omega - \Delta)] \quad (23)$$

to the inner side of the upper Hubbard band (not shown). Here $\Theta(x)$ denotes the Heaviside function, $P_n(x)$ is an n th order polynomial

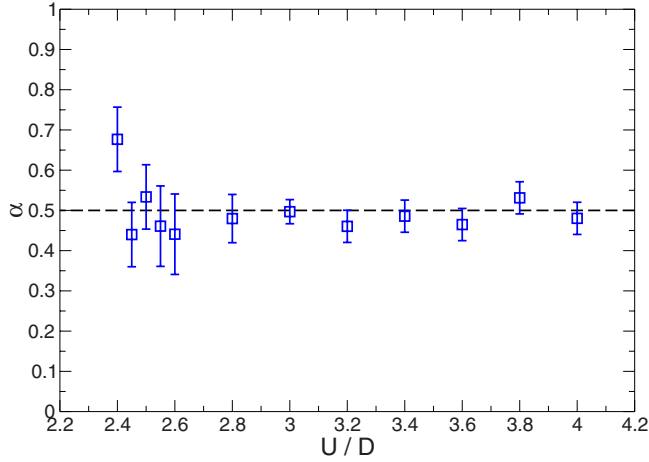


FIG. 6. (Color online) Leading exponent α in the behavior of the spectral density $\rho(\omega)$ near the band edges ($\omega \rightarrow \Delta$) for various values of U . The dashed line marks the value $\alpha=0.5$ suggested by perturbation theory (Ref. 32).

$$P_n(x) = \sum_{i=0}^n c_i x^i, \quad (24)$$

and α , Δ , and the c_i are the fit parameters. The parameter α represents the leading exponent of the power law onset. Note that a perfect square-root onset cannot be extracted using the LB deconvolution scheme since the ansatz for the unbroadened data is built from exponential functions.²³ Hence the fit results depend on a number of assumptions, for instance, the degree n of $P_n(x)$ and the interval in which the least-square fit is done. Figure 6 summarizes our results; the ambiguities are accounted for by the error bars. Our results excellently confirm the square-root onset. The agreement is very good for large values of the interaction, i.e., deep in the insulating regime. Closer to the closure of the gap the uncertainties grow.

The outer band edges of the Hubbard bands do not show any sharp decay. Instead, they reveal a smooth drop for $|\omega| \rightarrow \infty$ which becomes even smoother as U decreases, similar to the behavior of the metallic solutions, cf. Sec. III B.

2. Insulating gap

The gap Δ is the characteristic quantity of the insulator. Because of the impossibility to determine it directly from the LB deconvolved spectral density we use the value which is found from the fit (23) with fixed exponent $\alpha=1/2$. We stress that this determination of the gap Δ does not enter the iterations of the self-consistency cycle, except for the removal of artifacts, see Appendix B 2. It is done only at the end of the iterations once the solution can be considered to be self-consistent according to the criteria in Sec. II C 4. This is in contrast to the fixed-energy procedure chosen in Ref. 34 where the gap enters in the self-consistency explicitly. Again, it is *a priori* not clear which approach is more advantageous. All we found was that we could not reach stable self-consistency when using extrapolated gaps in the deconvolution.

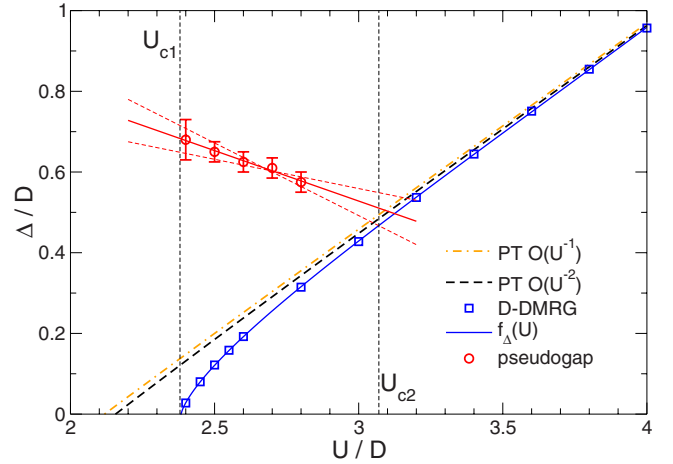


FIG. 7. (Color online) Single-particle gap Δ from the insulating solutions and the pseudogap from the metallic solutions vs the interaction U . The determination of the pseudogap is explained in Sec. III B. For comparison the results from perturbation theory (PT) up to $\mathcal{O}(U^{-2})$ in the insulating regime are also shown (Refs. 29 and 59).

The results are plotted in Fig. 7 as a function of U . As expected, the gap Δ decreases continuously with decreasing U until it vanishes at a critical value U_{c1} . For $U \geq 3.4D$ our $\Delta(U)$ agrees well with the results from perturbation theory expanding in powers of t/U .²⁹

Closer to the vanishing gap the behavior of $\Delta(U)$ is not linear anymore but displays a significant curvature. Qualitatively, this is similar to what has been observed previously in iterated perturbation theory³⁷ (IPT), by the local moment approach,³⁸ or by the Lanczos approach D-DMRG.³³ This observation leads us to fit a power law

$$f_{\Delta}(U) = (U - U_{c1})^{\zeta} [a_1 + a_2(U - U_{c1})] \quad (25)$$

with the fit parameters a_i , U_{c1} , and ζ , which denotes the leading exponent of $\Delta(U)$ close to U_{c1} . From this fit $U_{c1} = (2.38 \pm 0.02)D$ and $\zeta = 0.72 \pm 0.05$ is found. Thus, our value for U_{c1} agrees excellently with most of the previous results, see Table I.

3. Self-energy

The self-energy Σ is not required in the self-consistency cycle shown in Fig. 2, but it is accessible via Eqs. (3a) and (6). By means of the self-consistently determined full propagator $G(\omega)$ and the bare propagator $g^0(\omega)$ of the SIAM we compute

$$\Sigma(\omega) = \frac{1}{g^0(\omega)} - \frac{1}{G(\omega)}. \quad (26)$$

Note that this way to access the self-energy can be prone to numerical problems. If the self-energy is a small quantity it can acquire a substantial relative error if it is computed according to Eq. (26) as difference of two large quantities. In the extreme case, it can happen that the imaginary part of the retarded self-energy computed via Eq. (26) is positive, i.e., it displays the wrong sign and violates causality. This will be a

TABLE I. Comparison of the values for U_{c1} and U_{c2} found by various approaches.

U_{c1}/D	U_{c2}/D	Method
2.38 ± 0.02	3.07 ± 0.1	D-DMRG (CV, direct inversion)
2.225 ± 0.025	3.05 ± 0.05	D-DMRG (CV, variational) ^a
2.39 ± 0.02	3.0 ± 0.2	D-DMRG (Lanczos) ^b
2.39		PT-QMC ^c
2.39	2.94	NRG ^d
	3	linearized DMFT ^e
	2.92 ± 0.05	PSCM ^f

^aReferences 27 and 28.

^bReference 33.

^cReference 35.

^dReferences 46 and 47.

^eReference 56.

^fReference 48.

problem in the metallic solutions at weak coupling, see Sec. III B.

The indirectly calculated self-energy in the insulating regime displays the expected features, see Fig. 8. Except for a δ peak in the imaginary part at $\omega=0$, $\Sigma(\omega)$ is strictly real inside the gap

$$\text{Im } \Sigma(\omega) = -c\pi\delta(\omega) \quad \text{for } |\omega| \leq \Delta, \quad (27)$$

with $c > 0$. Correspondingly, the real part of $\Sigma(\omega)$ shows an $1/\omega$ behavior: $\text{Re } \Sigma(\omega) = c/\omega + \mathcal{O}(\omega)$.

4. Momentum-resolved spectral densities

So far we discussed the local spectral density $\rho(\omega)$ which is related to the imaginary part of the local propagator $G_{ii}(\omega)$. This is the quantity which matters in the self-consistency of the DMFT approach. However, once a self-consistent solution is found one can go a step further toward spatial correlations. While the self-energy and the skeleton diagrams are local in DMFT (see above) one-particle reducible quantities such as the propagators are not. Hence it makes sense to discuss G_{ij} . Because we study a translationally invariant system we study the propagator in momentum space $G_k(\omega)$.⁶⁰ Its Dyson equation reads

$$G_k(\omega) = \frac{1}{\omega - \epsilon_k - \Sigma(\omega)}. \quad (28)$$

By varying the bare fermionic energy ϵ_k we can assess the effect of different momenta. In particular, if we change ϵ_k from negative to positive values we can view the change of the single-particle response on passing from the dynamics of a hole to the one of an electron.

Figures 9 and 10 display the spectral density of $G_k(\omega)$ as follows:

$$\rho(\omega, \epsilon_k) := -\frac{1}{\pi} \text{Im } G_k(\omega). \quad (29)$$

Tiny wiggles in the intensity as function of the frequency are numerical artifacts of the self-energy computed via Eq. (26). The gap between the lower and the upper Hubbard bands is clearly visible. In each Hubbard band there is a ridge of high density running from the upper right to the lower left edge. Neglecting the strong scattering we can interpret this ridge as the dispersion of a moving double occupancy in the upper Hubbard band. Correspondingly, there is a moving empty site in the lower Hubbard band. Since the bandwidth of each Hubbard band is approximately equal to the bandwidth of the bare dispersion we deduce that the hopping of the double occupancy or the empty site, respectively, equals the bare hopping. This fact has been exploited also in the perturbative treatment.²⁹

Note, that the first approximation to this problem obtained by Hubbard¹² yields only *half* the bandwidth for each Hubbard band. However, the famous improved solution in Hubbard's third paper³⁹ displays the correct bandwidth for strong coupling. This treatment also includes scattering processes which take the strong scattering of the additional fermion into account. Hence it is very instructive to compare our numerically exact result with the approximate solution in Ref. 39. Figure 11 shows two examples for an almost vanishing gap at $U=1.8D$ and for a large gap at $U=4.0D$. The similarity to the exact results in Fig. 9, upper panel, and in Fig. 10, lower panel, is striking. Both results, exact and approximate, show strongly scattered, hence broadened, excitations in the Hubbard bands. The ridges behave very similarly in shape and height. In particular, for the large gap the results agree well.

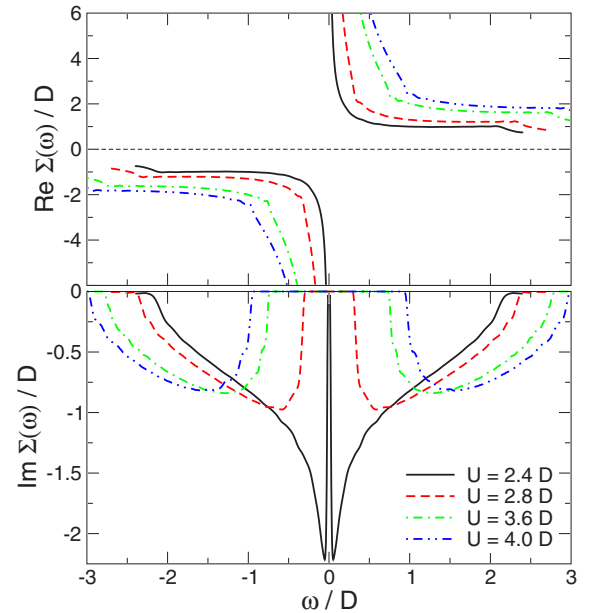


FIG. 8. (Color online) Real and imaginary parts of the self-energy $\Sigma(\omega)$ in the insulating regime. The δ peak in the imaginary part (lower panel) is not shown.

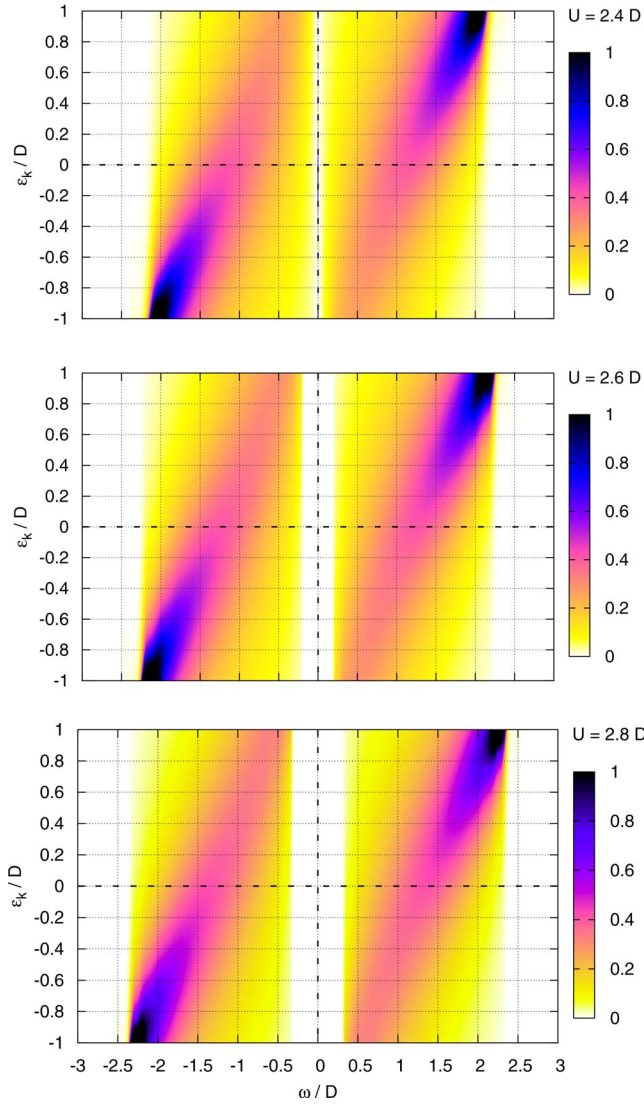


FIG. 9. (Color online) Spectral densities $\rho(\omega, \epsilon_k)$ in the insulating regime for $U=2.4D$ (top), $U=2.6D$ (middle), and $U=2.8D$ (bottom).

For the smaller value of the insulating gap, the most important difference is that the value of U differs. However, if we accept that the interaction value in Hubbard's approximation needs to be renormalized in a certain way the spectral densities behave qualitatively very similar. It must be stressed, however, that the results are quantitatively different. Comparing the upper left panel in Fig. 4 with the corresponding result in Ref. 39 one notes that the spectral weight in the exact solution is found further away from the Fermi level at $\omega=0$ while in Hubbard's solution it is shifted toward $\omega=0$.

B. Metal

1. Local spectral densities

Figure 12 shows the self-consistently calculated spectral densities $\rho(\omega)$ well in the metallic regime ($0 \leq U \leq 2D$). Fig-

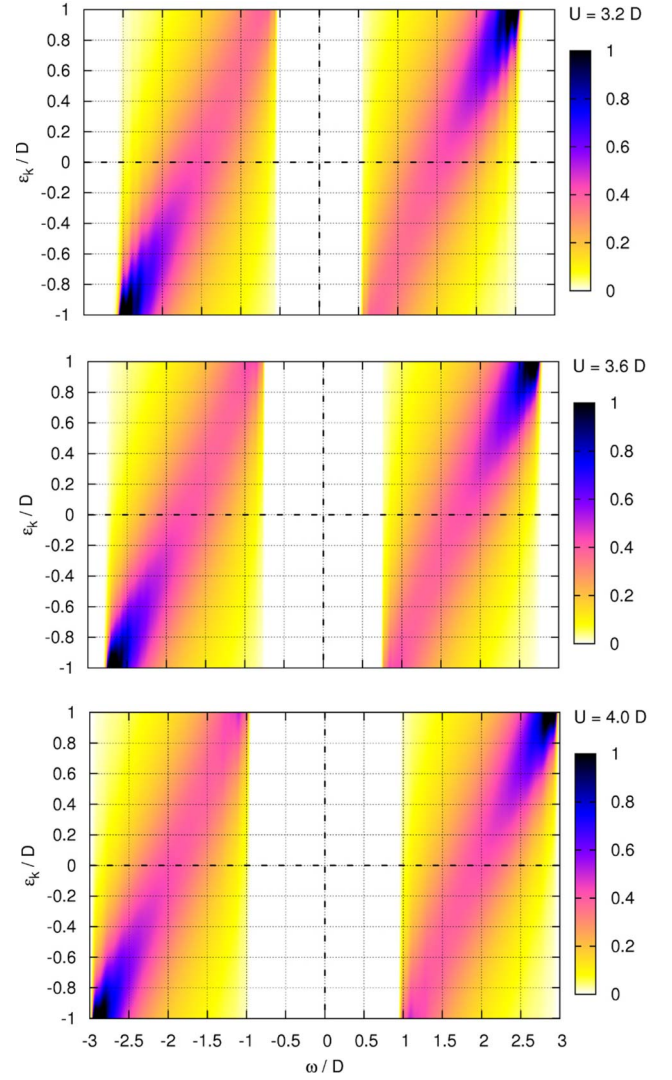


FIG. 10. (Color online) Spectral densities $\rho(\omega, \epsilon_k)$ in the insulating regime for $U=3.2D$ (top), $U=3.6D$ (middle), and $U=4.0D$ (bottom).

ure 13 shows the corresponding densities $\rho(\omega)$ closer to the transition to the insulating solution at $U=U_{c2} \approx 3.0D$. We used 160 fermionic sites (including one site representing the impurity) in the D-DMRG impurity solver. This implies a tiny bias toward the metallic solution, see Sec. II C 5. The raw data are obtained on an equidistant frequency grid with step size $\Delta\omega_i=0.1D$ using a constant broadening $\eta=0.1D$. It is deconvolved using the LB algorithm.²³ The spectral densities in Figs. 12 and 13 qualitatively display many of the features known from previous analytical^{29,32} and numerical^{4,33,41–47} investigations.

Starting from the semielliptic DOS (7) at $U=0$ the central peak becomes narrower and narrower on increasing U . The diminishing width is the Kondo energy scale T_K . The weight in the central peak is the quasiparticle weight Z which we will discuss below.

The height of the central peak does not change. The quasiparticle peak is pinned at the Fermi energy to its noninteracting value

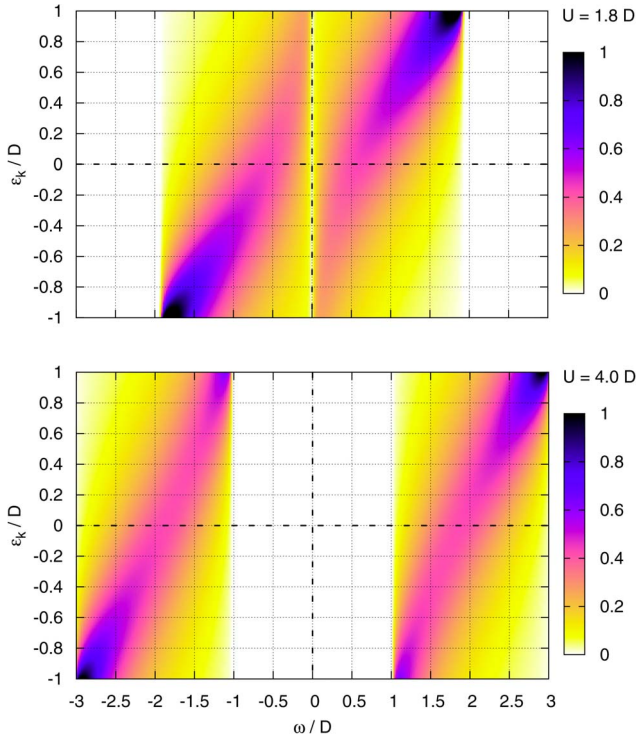


FIG. 11. (Color online) Spectral densities $\rho(\omega, \epsilon_k)$ in the insulating regime according to Hubbard's approximation in Ref. 39 for $U=1.8D$ (upper panel) and $U=4.0D$ (lower panel).

$$\rho(\omega=0) = \rho^0(\omega=0) = \frac{2}{\pi D}, \quad (30)$$

as required by Luttinger's theorem for a momentum independent self-energy.² As the DOS at zero frequency is not predetermined in our approach, the pinning criterion (30) provides a sensitive check for the accuracy of the numerical solutions in the metallic regime. This criterion is very well satisfied, see Fig. 12 and the upper panels in Fig. 13. A maximum relative error of 3% occurs for interaction values close to the transition to the insulator, see the lower panels in Fig. 13. The fulfillment of the pinning is an important prerequisite for an accurate determination of the quasiparticle weight Z below.

Beyond $U \approx D$, the DOS shows side features. They are just shoulders which develop into the lower and upper Hubbard bands at larger interaction. As expected, they appear roughly at $\omega = \pm U/2$. At $U \approx 2D$ the Hubbard bands are well separated from the quasiparticle peak by a precursor of the gap Δ in the insulator: a pseudogap is formed. This pseudogap is determined from $U=2.4D$ onward by background fits as shown in Fig. 17. The resulting values and their uncertainties are included in Fig. 7. Their extrapolation corroborates that the pseudogap evolves continuously to the insulating gap at $U_{c2} \approx 3D$ where the metallic solution becomes unstable toward the insulating solution.

The well pronounced pseudogap in the metallic solutions close to the transition reveals clearly that the quasiparticle peak becomes isolated from the Hubbard bands at higher

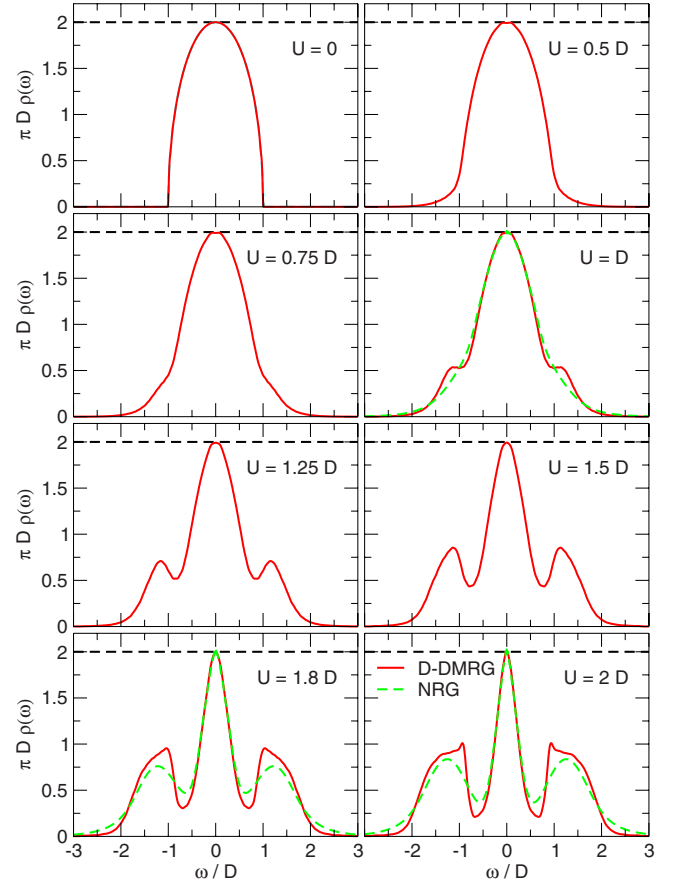


FIG. 12. (Color online) Spectral densities $\rho(\omega)$ in the metallic regime calculated with a chain of 160 fermionic sites. The dashed lines show results of a DMFT approach based on the numerical renormalization group (NRG) as impurity solver (Ref. 40).

energies. We demonstrated in Fig. 2 in Ref. 10 that the spectral densities of the metallic and of the coexisting insulating solution almost coincide at higher energies. This means that except for the quasiparticle peak and the inner edges of the Hubbard bands the insulating and the metallic solutions are almost identical. The two phases differ in their behavior at small and intermediate energies. This phenomenon has been baptized *separation of energy scales*. The assumption of its validity is at the basis of the numerical projective self-consistent method^{18,48} and of Kotliar's analytical Landau theory.¹⁴ Hence, the fact that our all-numerical treatment indeed displays the separation of energy scales represents a valuable confirmation of this important hypothesis.

It is very instructive to compare our findings for $\rho(\omega)$ with the numerical renormalization group (NRG) data from Ref. 40. The quantitative comparison is depicted in some of the panels in Figs. 12 and 13. The agreement is very good in the close vicinity of the quasiparticle peak, i.e., at low energies. However, significant deviations are discernible for intermediate and higher frequencies. The Hubbard bands obtained by the D-DMRG are sharper compared to the NRG results. Hence their precursors become visible already at lower values of U , see Fig. 12. Furthermore, the Hubbard bands in D-DMRG do not have significant tails at higher

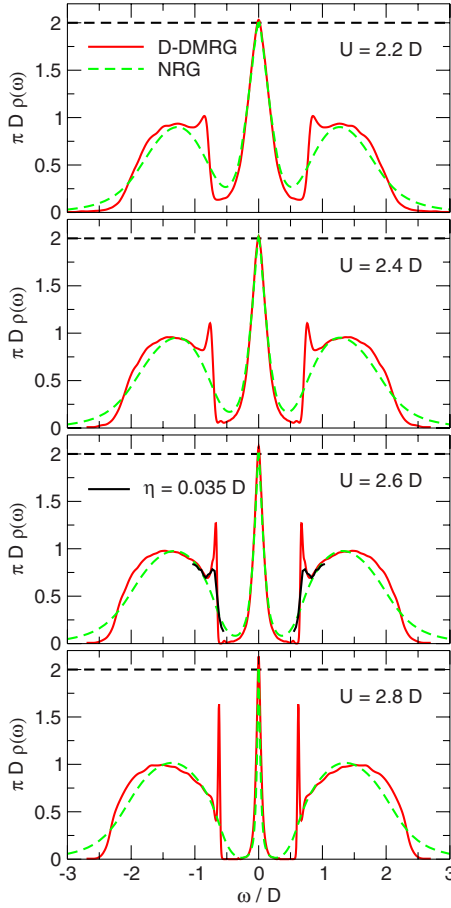


FIG. 13. (Color online) Spectral densities $\rho(\omega)$ in the metallic regime close to the metal-to-insulator transition. The dashed lines show results of an NRG-based DMFT approach (Ref. 40). For $U = 2.6D$, the dark solid lines show the raw D-DMRG data broadened with $\eta = 0.035D$ around the inner Hubbard band edges, for discussion see Sec. III B 2.

energies. This difference stems from the broadening proportional to the frequency which is inherent to the NRG algorithm.^{9,46,47,49,50} Similar differences were also reported in Ref. 32 where perturbative results are compared with NRG data.

In order to investigate a possible influence of finite-size effects, we consider the self-consistent spectral densities and the associated bath parameters γ_n , cf. Eq. (15), for various sizes of the bath. Figure 14 shows the results for $L=120$, 160, and 240 fermionic sites well in the metallic regime for $U=D$ and $U=2D$. If the finite broadening of the D-DMRG raw data is chosen according to Eq. (19) the spectral densities deconvolved by LB are not affected significantly by the number of bath sites. We observe neither qualitative nor significant quantitative differences. This observation applies also to the self-consistently determined bath parameters γ_n . Above $n \approx 80$ almost all bath parameters take the same value which determines the bandwidth, see Appendix A.

We conclude that a system size of 80 fermionic sites is already sufficient to capture quantitatively the features of the spectral properties well in the metallic regime. Nevertheless, a small improvement in the pinning criterion can be observed

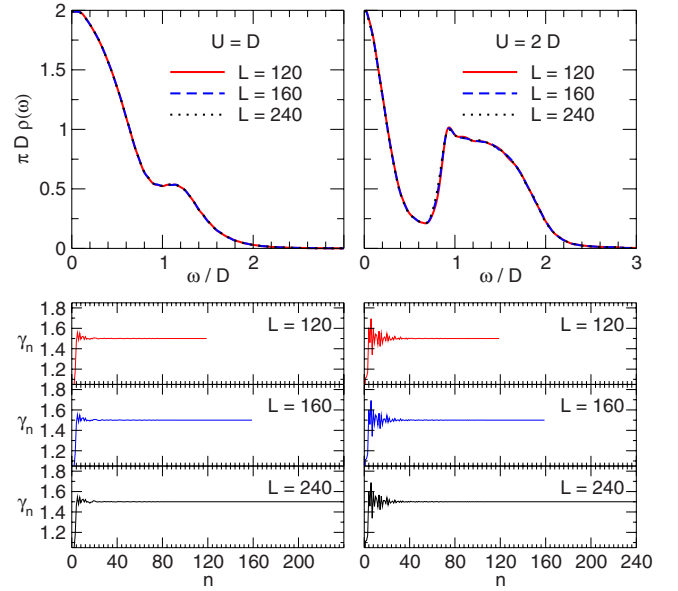


FIG. 14. (Color online) Part of the spectral density $\rho(\omega)$ and the associated bath parameters γ_n calculated self-consistently for various numbers L of fermionic sites. Left panel: $U=D$. Right panel: $U=2D$.

if more fermionic sites are considered, see Ref. 15. This improvement arises from a better approximation of the thermodynamic limit which makes the deconvolution using the LB algorithm more robust. However, the system size cannot be chosen too large in practice because the D-DMRG calculation will acquire systematic errors for large systems and given computational resources. Our D-DMRG calculations were all done with 128 states, partly checked by runs with 256 states. However, we have not noticed significant deviations between the runs with 128 and those with 256 states.

2. Sharp inner side peaks

For strong interactions ($U > 2D$) close to the metal-to-insulator transition the metallic solutions show sharp peaks at the inner edges of the Hubbard bands, see Fig. 12 for $U = 2D$ and Fig. 13. These peaks become sharper and sharper on increasing the interaction U . Note that their height cannot (and does not) exceed the maximum value of the noninteracting DOS because the interacting DOS is determined from the Dyson equation (4). It implies that $\rho(\omega)$ results from $\rho^0(\omega)$ by a shift in frequency due to $\text{Re} \Sigma$ and by a Lorentzian broadening due to $\text{Im} \Sigma$ so that $\rho(\omega)$ is bounded by the maximum of $\rho^0(\omega)$. The sharp features do not represent diverging singularities.

In order to properly resolve the sharp side peaks as well as the narrow quasiparticle peak, we choose $\Delta\omega_i = \eta_i = 0.05D$ and partially $\Delta\omega_i = \eta_i = 0.025D$ in the relevant frequency regions. Furthermore, we place the computed points of the raw data at the frequency of the maximum of the side peaks.

In Fig. 15 we show that the sharp peaks at the inner band edges are not an artifact of the deconvolution algorithm since a large variety of deconvolution schemes essentially provides

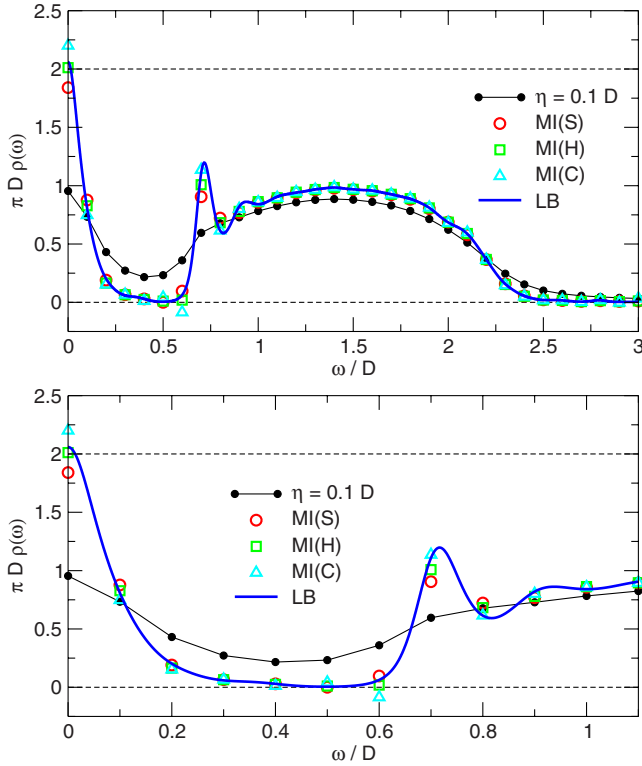


FIG. 15. (Color online) Comparison of various deconvolution schemes for $U=2.6D$. The solid line with filled circles depicts the raw data. MI refers to linear matrix inversion for which we assume that the DOS consists of a set of δ functions [spikes, MI(S): circles] or that it is piecewise constant [histogram, MI(H): squares] or that it is piecewise linear and continuous [MI(C): triangles], for details see Ref. 23. LB stands for the continuous positive result obtained by the nonlinear LB deconvolution. Upper panel: complete frequency interval of the symmetric DOS. Lower panel: details at lower frequencies.

the same peak. Furthermore, the side peaks are already discernible in the raw data at small broadening (dark solid lines) shown in Fig. 13 for $U=2.6D$.

We checked that different initial hybridization functions led to the same self-consistent solutions after sufficient iterations so that we exclude that the side peaks are artifacts of the self-consistency procedure. Moreover, Nishimoto *et al.* found very similar side peaks by a completely independent implementation of DMFT by D-DMRG.²⁸ Hence we conclude that the sharp side peaks resolved in our D-DMRG approach are part and parcel of the metallic spectral density of the half-filled Hubbard model close to the metal-to-insulator transition.

We repeated the investigation of the possible influence of the system size in Fig. 14 close to the metal-to-insulator transition. In Fig. 16 we compare spectral densities for $U=2.4D$ and $U=2.6D$ and their bath parameters γ_n determined self-consistently for 120, 160, and 240 fermionic sites with $\Delta\omega_i = \eta_i = 0.1D$. Smaller values for $\Delta\omega$ and η turned out not to be feasible for the large system sizes due to limited computational resources. Thus, we accept a slight loss in the resolution of the side peaks compared to the spectral densities shown in Fig. 13 where calculations with $\Delta\omega_i = \eta_i$

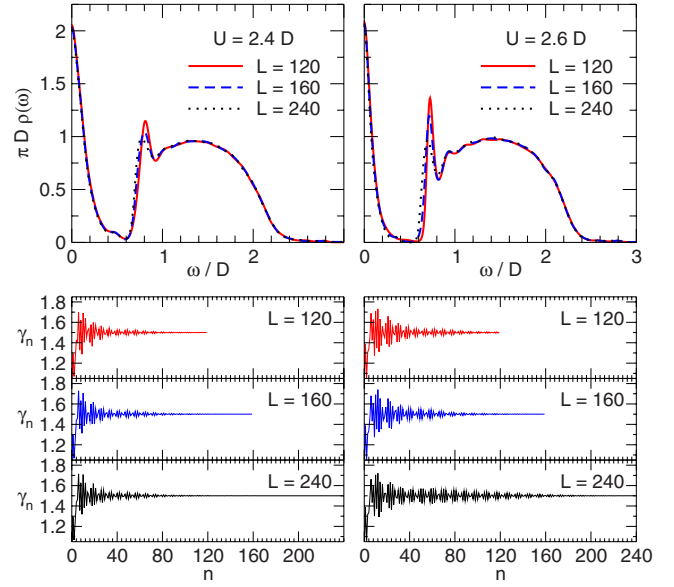


FIG. 16. (Color online) Part of the spectral density $\rho(\omega)$ and the associated bath parameters γ_n calculated self-consistently for various numbers L of fermionic sites. Left: $U=2.4D$. Right: $U=2.6D$.

$=0.025D$ were performed for frequencies around the side peak positions.

We see in Fig. 16 that the precise position and the shape of the side peaks depend slightly on the size of the bath considered in the numerical calculations. The other, less sharp features, such as the central peak and the Hubbard band, are very robust against the changes of the bath size. It is very instructive to look at the bath parameters γ_n . For $U=2.4D$ they do not change on passing from $L=120$ over $L=160$ to $L=240$. The oscillations visible from smaller values of $n \lesssim 80$ are essentially the same for the three system sizes. They do not extend to larger n for larger L . For $U=2.6D$, however, the bath parameters change for larger systems. The oscillations extend to higher n for $L=240$ than for lower L . For $L=240$ they appear to have converged for large n so that we assume that increasing L further would only extend the region of almost constant γ_n .

We conclude that sufficiently large baths are essential for a quantitative description of the spectral densities and of the sharp features at the inner edges of the Hubbard bands, in particular. This is especially important close to the metal-to-insulator transition. Our results confirm the existence of the sharp side peaks and provide their accurate determination for all $U \leq 2.2D$. For $U > 2.2D$ the possibility of small inaccuracies of the order of the deviations shown in the upper panels of Fig. 16 must be kept in mind.

The only previous evidence for sharp side peaks in numerical investigations were weak shoulders in NRG⁴⁶ and quantum Monte Carlo (QMC)⁵¹ data. The inherent broadening in the NRG calculations and the necessity to continue the QMC data from imaginary times to real frequencies have both a tendency to smear out sharp features away from the Fermi level, cf. Ref. 9. Hence we tend to interpret the shoulders in Refs. 46 and 51 as broadened remnants of the sharp peaks resolved in the present D-DMRG calculation.

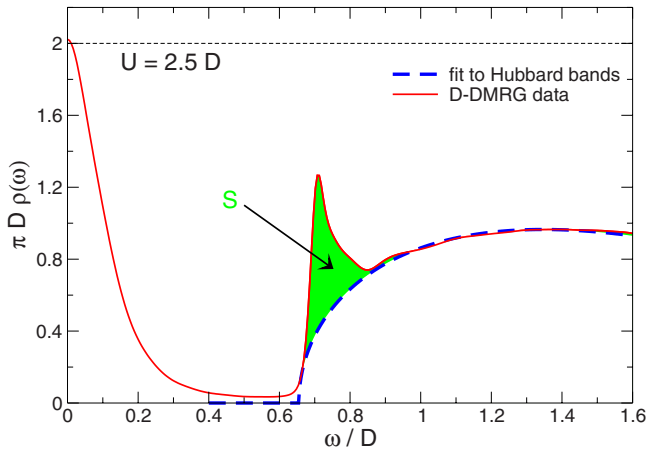


FIG. 17. (Color online) Determination of the side peak weight S illustrated for $U=2.5D$.

Besides the numerical approaches, semianalytical approaches, the IPT¹⁸ and the noncrossing approximation (NCA),⁵² display similar behavior of the spectral densities near the inner Hubbard band edges. The IPT results show a substantial accumulation of spectral weight at the inner band edges which differs very much from our findings: the weight is much larger and the features are by far not as sharp as those presented here. They carry even more spectral weight than the quasiparticle peak and they are accompanied by spike structures over the entire Hubbard bands in contrast again to our findings. In view of these differences and because IPT is an approximate diagrammatic approach we conclude that the IPT features do not correspond to the ones presented here.

The NCA data in Ref. 52 is qualitatively much closer to our data as far as the side peaks are concerned. Since the NCA violates the Fermi liquid properties for temperatures lower than the Kondo scale⁵³ reliable conclusions can only be drawn for sufficiently large temperatures. Moreover, the peaks are found in the insulating phase so that it is an open question whether the NCA findings are related to the D-DMRG side peaks at zero temperature in the metallic regime.

In order to pave the way to a physical interpretation of the side peaks we determine its weight S . Motivated by the results for insulating $\rho(\omega)$ in Sec. III A 1 we fit an approximate square-root onset multiplied by a quadratic polynomial to the Hubbard band. The excess weight is identified with the spectral weight S of the sharp side peak. This procedure is illustrated in Fig. 17.

Inspection of Fig. 13 suggests that S vanishes for $U \rightarrow U_{c2}$. This conclusion is supported by the fact that the insulating solutions do not display a similar feature, see Sec. III A 1. Hence we presume that the side peak involves quasiparticles from the central peak. The weight in this central peak is given by Z which vanishes linearly for $U \rightarrow U_{c2}$, see Sec. III B 4. So we plot the results for S as function of Z in Fig. 18 including a point $S=0$ for $Z=0$. The error bars result from the numerical difficulty to resolve this sharp feature and from the analytical difficulty to separate it from the background of the Hubbard bands.

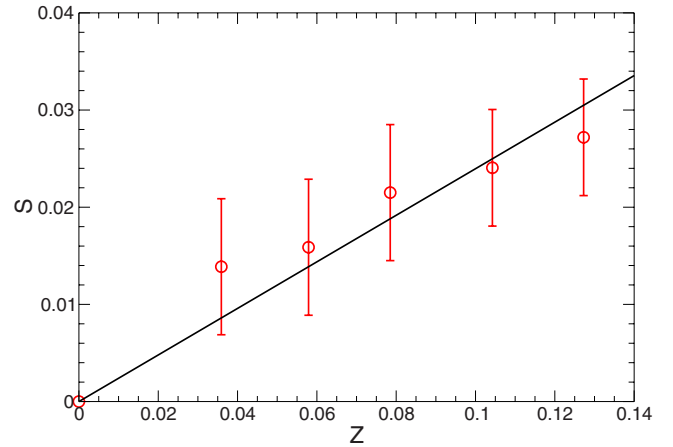


FIG. 18. (Color online) Weight S of the peaks at inner Hubbard band edges as a function of the quasiparticle weight Z .

In view of the errors the interpretation of Fig. 18 is daring. However, our guiding hypothesis is that the surprisingly sharp side peak is the signature of a composite excitation involving several fermionic excitations.¹⁰ A single quasiparticle alone cannot be at the origin of a sharp feature because it has a finite dispersion and a finite lifetime so that it engenders only broad features in local quantities away from the Fermi level.

One possible assumption is that the composite excitation comprises three quasiparticles (note that the total statistics must be fermionic). However, they need to be bound or antbound to account for the very sharp structure which tells us that the composite entity must be almost immobile. Otherwise it would give rise only to a broad structure in local spectral densities, which correspond to sums over the entire Brillouin zone. A plausible second scenario is that a single quasiparticle is combined with a collective mode, for instance, a particle-hole pair as it occurs when a spin is flipped.

With these ideas in mind, we want to use Fig. 18 only to decide whether one, two, or three quasiparticles are involved. The quasiparticle weight Z measures to which extent a local fermionic creation operator generates a true quasiparticle including its polarization dressing. So we presume that the contribution of a single quasiparticle gives rise to a linear behavior $S \propto Z$ while two quasiparticles lead to $S \propto Z^2$, and three quasiparticles imply $S \propto Z^3$. Hence we find in the linear fit in Fig. 18 a hint that only one quasiparticle contributes to the side peaks.

Additionally, we presume that an immobile collective mode is involved. Note that due to the scaling (2) in DMFT collective modes are as such immobile because their motion requires at least *two* single-particle propagators. The nature, however, of the collective mode inducing the composite feature is still an open issue which we address in ongoing investigations.

3. Self-energy

In the metallic phase we again use Eq. (26) to obtain the self-energy. The results are plotted in Fig. 19. The real and imaginary parts of the self-energy display a typical low-

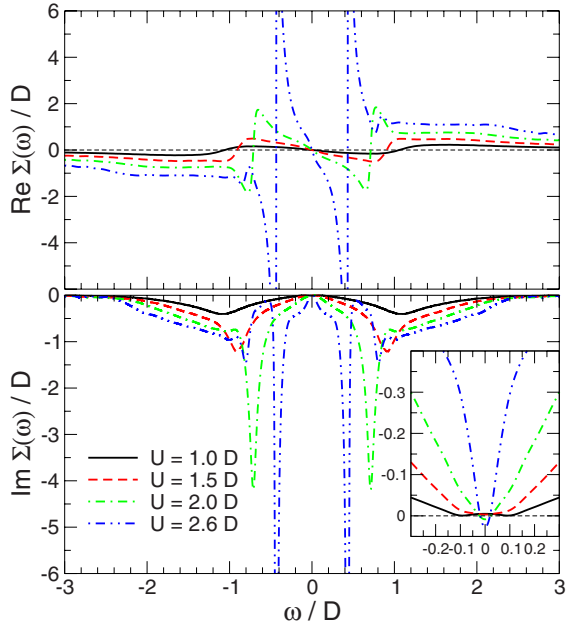


FIG. 19. (Color online) Real and imaginary parts of the self-energy $\Sigma(\omega)$ in the metallic regime. Inset: $\text{Im } \Sigma(\omega)$ on a larger scale.

frequency behavior of a local Fermi liquid: The real part shows a linear behavior with a negative slope which steepens as U increases. In this region, the imaginary part of $\Sigma(\omega)$ shows a quadratic behavior, $\text{Im } \Sigma(\omega) \propto -\omega^2$, as expected.² The quadratic behavior of $\text{Im } \Sigma$ is not perfectly retrieved, see inset of Fig. 19. For low values of U it seems that $\text{Im } \Sigma$ is proportional to a higher power than ω^2 for $\omega \rightarrow 0$. For large interaction values, for instance, $U=2.6D$, the computation of the self-energy via Eq. (26) even leads to negative spectral densities (positive $\text{Im } \Sigma$ for the retarded self-energy) violating causality. This is a clear indication for the limits of the accuracy of the present calculation. However, we stress that these difficulties are minor and do not affect the self-consistency because they occur only when the self-energy is computed from the full propagator G .

The two-peak structure in the imaginary part of $\Sigma(\omega)$ is closely related to the three-peak structure of the spectral density given by the lower Hubbard band, central Kondo peak, and the upper Hubbard band. According to Eq. (26) the self-energy has a peak if the real and imaginary parts of $G(\omega)$ are small. For the metallic solutions, this is the case in the frequency regime between the Hubbard bands and the quasiparticle peak, i.e., within the pseudogap.

This relation has been previously analyzed.^{46,54,55} It turns out that the strong peaks in the self-energy are located at position $\omega_{\Sigma} \propto \pm \sqrt{ZD}$, where Z is the quasiparticle weight, see next subsection. Our data agrees very well with the analytical arguments; the factor of proportionality is about $\sqrt{2}$. We stress that $\omega_{\Sigma} \rightarrow 0$ on approaching the metal-to-insulator transition whereas the sharp inner side peaks remain at the inner band edges. Hence the two peaks in the imaginary part of the self-energy are not directly related to the sharp side peaks. It should be pointed out that the two-peak structure of the self-energy contradicts the findings in Ref. 55. We pre-

sume that the analytical argument misses some effect which requires further research.

4. Quasiparticle weight

The quasiparticle weight Z is the characteristic quantity of the metallic phase. Crudely speaking Z quantifies how much of the spectral weight is found in the central quasiparticle peak, cf. Figs. 13 and 12. In other words, Z is the matrix element between the fermionic creation operator applied to the ground state and the dressed quasiparticle excitation including its polarization cloud. For local self-energies² it is given by

$$Z^{-1} = 1 - \partial_{\omega} \Sigma(\omega)|_{\omega=0}. \quad (31)$$

Because the self-energy is not directly accessible in our approach we prefer to calculate Z using the derivative of the Dyson equation (4) implying

$$Z^{-1} = \frac{D^2}{2} \partial_{\omega} G(\omega)|_{\omega=0}, \quad (32)$$

where $\partial_{\omega} G^0(\omega)|_{\omega=0} = 2/D^2$ has been used. By Eq. (32) we avoid the numerical errors occurring if the self-energy is determined via Eq. (26), see Sec. III B 3.

The derivative $\partial_{\omega} G(\omega)|_{\omega=0}$ in Eq. (32) is real because the imaginary part displays an extremum at $\omega=0$. The derivative of $\text{Re } G(\omega)$ is obtained reliably from the coefficient a of the fit function

$$f_{\text{Re } G}(\omega) = a\omega + b\omega^3, \quad (33)$$

where the absence of even orders due to particle-hole symmetry has been taken into account. The fit is done in the intervals around the origin which decrease for $U \rightarrow U_{c2}$ roughly linearly; for $U=2D$ it is $[-0.1D, 0.1D]$. The derivative cannot be determined robustly as ratio of differences because $\text{Re } G(\omega)$ displays weak oscillations resulting via the Kramers-Kronig transformation from weak wiggles in $\text{Im } G(\omega)$ due to the deconvolution procedure; see, for instance, the lowest panel in Fig. 13 around $\omega=D$.

In Fig. 20 the quasiparticle weight Z is depicted as a function of U . Starting from $Z=1$ at $U=0$, Z decays as U increases. Our results agree excellently with perturbation theory where it is applicable $U \lesssim D$. The NRG data are lower for all values of U . We deduce that the broadening of the spectral weights proportional to ω , inherent to NRG, has a non-negligible influence on the quasiparticle weight. Qualitatively, however, the behavior of $Z(U)$ is very similar.

From the trend of $Z(U)$ one expects that Z vanishes continuously at a finite critical value U_{c2} . We cannot approach this value arbitrarily closely because the reliable resolution of the sharper and sharper quasiparticle peak would require a better and better resolution. This in turn cannot be achieved with a reasonable amount of computing resources because Eq. (19) must be respected. For this reason, we have to resort to an extrapolation to determine U_{c2} quantitatively.

The behavior of $Z(U)$ close to U_{c2} was already investigated previously analytically by the projected self-consistent method (PSCM)⁴⁸ and by the linearized DMFT.⁵⁶ Both meth-

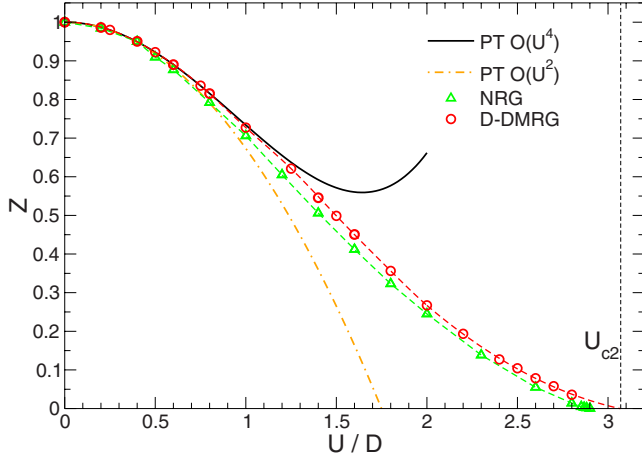


FIG. 20. (Color online) Quasiparticle weight Z as a function of U compared to perturbative results (Ref. 32) (PT) up to $\mathcal{O}(U^4)$ and to NRG data (Ref. 46).

ods assume the separation of energy scales and predict a linear behavior of Z close to U_{c2} . Since our all-numerical spectral densities strikingly confirm the separation of the energy scales¹⁰ we determine U_{c2} by fitting

$$f_Z(U) = a_1(U - U_{c2}) + a_2(U - U_{c2})^2 \quad (34)$$

to the data points for $U \in [2, 2.8]D$. We obtain a critical value of $U_{c2} = (3.07 \pm 0.1)D$ which agrees excellently within the error range with most of the previous results,^{33,35,36,46–48,56} including the linearized DMFT⁵⁶ and the PSCM.⁴⁸ For comparison, we include an overview of these critical values in Table I.

5. Momentum-resolved spectral densities

For the metallic phase, we present spectral densities $\rho(\omega, \epsilon_k)$ as defined in Eqs. (28) and (29) which are resolved according to their bare single-particle energy ϵ_k . In the context of the DMFT, this procedure provides information on the momentum dependence of the spectral properties. Figures 21 and 22 display how the momentum-resolved spectral densities evolve on approaching the metal-to-insulator transition.

Three main features can be discerned. First, the dominant diagonal line of highest intensity with $\omega_{\text{high}} \propto \epsilon_k$ catches our attention in all six panels. This is where the Fermi liquid picture manifests itself.⁵⁷ Without interaction a quasiparticle can be excited at $\omega_{\text{high}} = \epsilon_k$. In the presence of interaction there are still quasiparticles which behave like fermions above the Fermi level or holes below it. However, these excitations are dressed by clouds of particle-hole pairs. This dressing has two effects. One is that the bare fermionic operator has only an overlap reduced by Z with the creation of the quasiparticle. The other effect is that the dressed quasiparticles are heavier than their bare counterparts. This means that their dispersion is reduced. For a momentum-independent self-energy the reduction of the dispersion is given again by the factor $Z \leq 1$. This can be seen in the impressive steepening of the dominant diagonal line given by $\omega_{\text{high}} = Z\epsilon_k$ upon increasing interaction. For interaction

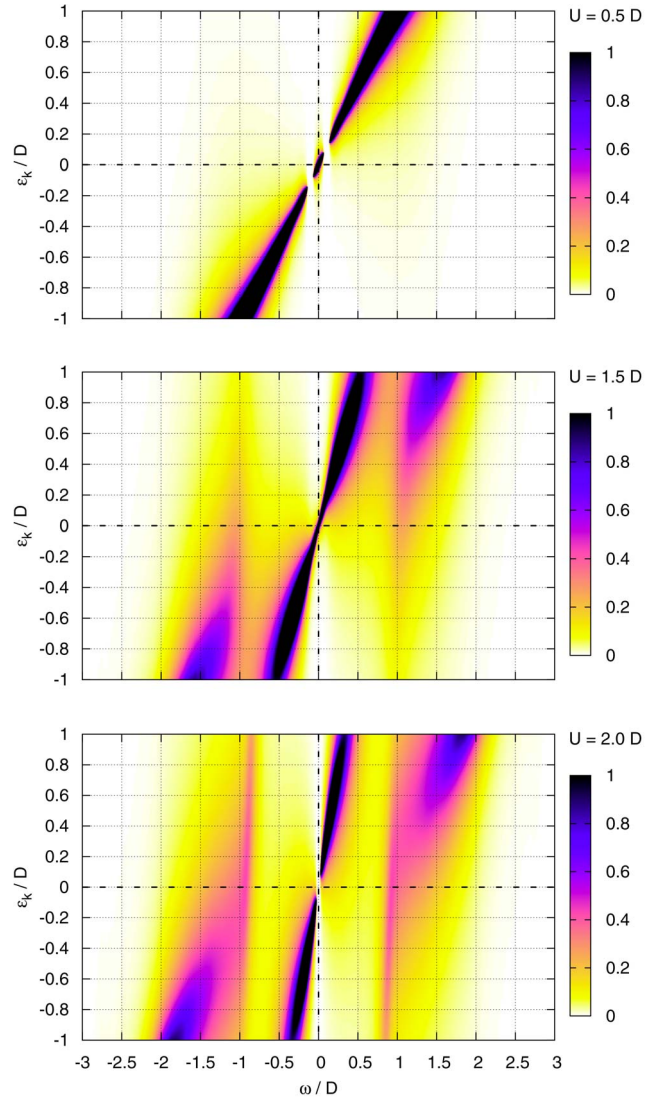


FIG. 21. (Color online) Spectral densities $\rho(\omega, \epsilon_k)$ in the metallic regime for $U=0.5D$ (top), $U=D$ (middle), and $U=2D$ (bottom).

values close to the instability of the metallic solution, see lowest panel in Fig. 22, the diagonal line has become so steep that it can almost be taken as a vertical one. This implies that the quasiparticle has become almost local and non-dispersive. This is the mechanism leading to the so-called heavy fermions.

We point out that the white stripes at $\omega=0$ in most of the panels in Figs. 21 and 22 and the white stripes at small ω in the first panel of Fig. 21 result from the numerical violations of causality as discussed before, see Secs. III A 3 and III B 3. For values of ω where this problem occurs the spectral densities are set to zero.

The second main feature in the momentum-resolved spectral densities is the development of the precursors of the lower and upper Hubbard bands. At $U=0.5D$ no such precursors are visible, except for some broadening of the diagonal line away from the Fermi level. However, in the panel for $U=1.5D$ the precursors are already clearly visible. They are qualitatively very similar to the broad densities found in the

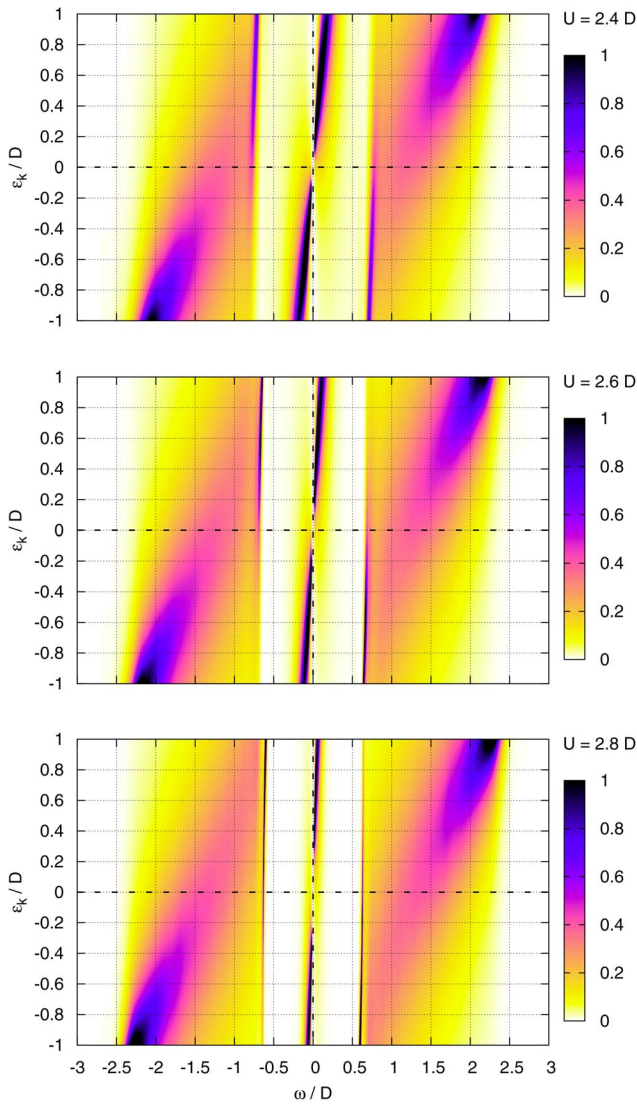


FIG. 22. (Color online) Spectral densities $\rho(\omega, \epsilon_k)$ in the metallic regime for $U=2.4D$ (top), $U=2.6D$ (middle), and $U=2.8D$ (bottom).

insulating spectral densities in Figs. 9 and 10. This similarity becomes more and more pronounced as U approaches U_{c2} where the metal changes continuously to the insulator.

The third main feature is the occurrence of a vertical line of high density at the inner edges of the precursors of the Hubbard bands. It is barely visible for $U=2.0D$, see last panel of Fig. 21. However, it is clearly discernible for the larger values of the interaction displayed in Fig. 22. This vertical line represents the momentum-resolved feature of the sharp side peaks at the inner band edges discussed in Sec. III B 2. We reemphasize that there is no discernible momentum dependence indicating a local, nondispersive, immobile excitation.

We draw the reader's attention to the fact that the vertical lines display an interesting dependence of their weight on the momentum. The high density is found for $\omega > 0$ for $\epsilon_k < 0$ and vice versa ($\omega < 0$ for $\epsilon_k > 0$). This implies that the immobile composite entity is excited upon adding a bare fer-

mion ($\omega > 0$), but for momenta corresponding to occupied states ($\epsilon_k < 0$) and vice versa. We deduce that the addition of the bare fermion must induce the creation of a quasiparticle hole, cf. Sec. III B 2. Further work to elucidate this puzzling behavior is called for.

IV. SUMMARY

The present work constitutes the comprehensive analysis of the transition from a metal to an insulator driven by strong repulsive interaction. The framework of this investigation is the dynamic mean-field theory (DMFT). We evaluate the necessary self-consistency equations at zero temperature with a numerical impurity solver based on dynamic density-matrix renormalization (D-DMRG). The D-DMRG computes a frequency-dependent correction vector which ensures a high reliability of the results at all energies, not only close to the Fermi level. Thereby, we are able to provide spectral densities in the metallic and in the insulating phase with unprecedented resolution. Such densities are relevant to photoelectron spectroscopy of transition metal compounds and other narrow-band systems.

The calculations are done for a semielliptic noninteracting density of states (DOS). All the important technical details of the intricate combination of D-DMRG and DMFT are given in detail so that our findings may be reproduced independently.

The local, momentum-integrated, spectral density in the insulating phase is governed by the lower and upper Hubbard bands. Both are featureless and display square-root singularities at the inner band edges. The insulating gap Δ vanishes continuously for $U \rightarrow U_{c1} = (2.38 \pm 0.02)D$. A slight curvature indicates that $\Delta \propto (U - U_{c1})^\zeta$ with $\zeta = 0.72 \pm 0.05$.

For $U < U_{c2} = (3.07 \pm 0.1)D$ the insulating solution is only metastable. The phase with lower ground-state energy is the metallic one.¹⁰ The corresponding spectral densities show three important features for significant interaction values: (i) the central quasiparticle peak, (ii) the precursors of the lower and upper Hubbard bands, and (iii) the sharp side peaks at the inner band edges of the Hubbard bands.

The DOS of the central peak at the Fermi level is pinned to its noninteracting value due to Luttinger's theorem. The central peak is built from heavy fermions or holes which disperse only weakly due to their strong dressing. They are the characteristic signature of a Fermi liquid.

The Hubbard bands signal that the metal evolves toward an insulator on increasing interaction. Our findings, both the earlier ones¹⁰ and the present ones, clearly show that the metallic spectral densities evolve continuously to the insulating one upon $U \rightarrow U_{c2}$. This continuity holds in the sense of an integral norm, i.e., considering the distribution of spectral weight, not in the sense of an absolute value norm which jumps. For instance, the DOS at the Fermi level is $2/(\pi D)$ in the metallic regime and 0 in the insulating one. However, the corresponding *weight* vanishes linearly for $U \rightarrow U_{c2}$. The pseudogap develops simultaneously to the insulating gap. These findings numerically confirm the assumption of the separation of energy scales.^{14,48}

The sharp side peaks at the inner edges of the Hubbard bands in the metallic regime are the signature of a complex composite excitation which is not yet understood. We found that its weight scales with the quasiparticle weight which supports our hypothesis that the side peaks stem from an entity made from a quasiparticle and some collective, immobile mode. The analysis of the momentum-resolved spectral densities shows in addition that the involved quasiparticle is a hole if a bare electron is added. Conversely, it is a particle if a bare hole is created, i.e., an electron is taken out.

Ongoing research is devoted to the nature of the composite excitation which generates the sharp side peaks. To this end, the response functions, which correspond to various collective modes, need to be investigated.

Other interesting issues concern the qualitative and quantitative dependences of the important features found on the noninteracting density of states. The changes introduced by doping certainly will be of particular interest. A first study, based on Lanczos-DMRG, of the effects of doping has been published very recently.⁵⁸

ACKNOWLEDGMENTS

We thank R. Bulla for the kind provision of the NRG data and F. B. Anders, P. Grete, S. Kehrein, and A. Lichtenstein for helpful discussions. The DFG is thanked for financial support in SFB 608 during the beginning of this project.

APPENDIX A: CALCULATION OF THE CONTINUED FRACTION COEFFICIENTS

Once a propagator $g(\omega)$ is known on a dense mesh of frequencies (about 10^5 points), one is able to determine its continued fraction representation to an arbitrary depth

$$g(\omega) = \frac{b_0^2}{\omega - a_0 - \frac{b_1^2}{\omega - a_1 - \frac{b_2^2}{\omega - a_2 - \dots}}} \quad (\text{A1})$$

very precisely. Numerically, only integrations are involved.

For the iteration, we define recursively the resolvents

$$p_0(\omega) := g(\omega), \quad (\text{A2a})$$

$$p_{n+1}(\omega) = \omega - a_n - \frac{b_n^2}{p_n(\omega)}. \quad (\text{A2b})$$

Obviously, the continued fraction representation of $p_n(\omega)$ starts with a_n and b_n . It is shifted by n relative to the continued fraction of g . An expansion in $1/\omega$ reads

$$p_n(\omega) = \frac{b_n^2}{\omega} \left[1 + \frac{a_n}{\omega} + \mathcal{O}(\omega^{-2}) \right]. \quad (\text{A3})$$

Comparing this expression with the expansion in $1/\omega$ of the Hilbert representation of $p_n(\omega)$ (Refs. 20 and 31) leads to

$$b_n^2 = -\frac{1}{\pi} \int_{-\infty}^{\infty} d\omega \operatorname{Im} p_n(\omega), \quad (\text{A4a})$$

$$a_n = -\frac{1}{\pi b_n^2} \int_{-\infty}^{\infty} d\omega \omega \operatorname{Im} p_n(\omega). \quad (\text{A4b})$$

The iteration of the above equations for $n=0,1,2,\dots$ yields the wanted coefficients. The iterations are stopped once all the coefficients for the numerically tractable finite chain of L fermionic sites are determined, i.e., for $n=L-3$.

In the case of a particle-hole symmetric model, the spectral density is symmetric. Consequently, all odd moments and thus all the coefficients a_n ($n=0,1,\dots$) vanish in the above recursion scheme. So for the model under study we need only to consider the equations for the b_n .

The asymptotic behavior of the continued fraction coefficients for $n \rightarrow \infty$ is determined by the bandwidth of the spectral density $\rho(\omega)$ and by the singularities at the band edges.^{20,31} We exploit the relation for the bandwidth $2B$, if the support of the spectral density is compact, which reads

$$4|b_\infty| = 2B, \quad (\text{A5})$$

where $b_\infty := \lim_{i \rightarrow \infty} b_i$. For a gap Δ in the middle of the spectral density, i.e., for the insulator, the b_i are oscillating for large i like

$$b_i \rightarrow b_\infty \pm (-1)^i \Delta/2, \quad (\text{A6})$$

where b_∞ is again given by a quarter of the bandwidth which is the distance between the largest and the smallest band edge including the gap.

In a strict sense we expect that the support of the spectral density of an interacting system is infinitely large. However, it turns out that significant spectral weight is found only in a finite interval. The contributions outside this interval are negligible which has been observed also in other calculations.²⁹

We use the relations (A5) and (A6) to determine the interval in which we have to compute raw data $\{g_i\}$. For this purpose we compute b_∞ in each iteration of the self-consistency cycle and observe its development on iteration. If the value of b_∞ does not change significantly for several iteration steps, we fix the border B of the interval in which we perform the calculation of the raw data. This procedure allows us to avoid the time-consuming calculation of unnecessary data points.

In the presence of an insulating gap Δ at the Fermi energy the above recursion schemes (A4a) and (A4b) to determine the continued fraction coefficients have to be modified for practical reasons. Due to the antisymmetry of its real part the propagator in the particle-hole symmetric case vanishes at $\omega=0$ completely $p_0(\omega=0)=0$ with no imaginary part. So there is a pole in $p_1(\omega)$ at $\omega=0$ according to (A2b) implying a finite contribution from a δ distribution at $\omega=0$ in $\operatorname{Im} p_1$. We account for it separately

$$b_1^2 = -\frac{1}{\pi} \int_{-\infty}^{\infty} d\omega \operatorname{Im} p_1(\omega) = -\frac{1}{\pi} \int_{\mathbb{R} \setminus [-\Delta, \Delta]} d\omega \operatorname{Im} p_1(\omega) + \frac{b_0^2}{|p_0'(0)|}. \quad (\text{A7})$$

The recursion relation (A2b) implies that the same scenario occurs for every odd n . So we use Eq. (A7) for any odd n

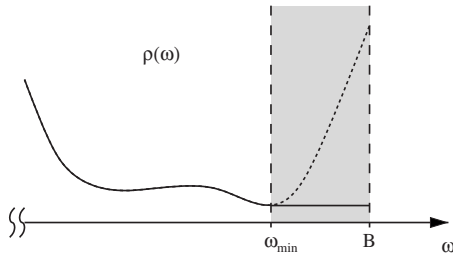


FIG. 23. Lines: generic deconvolved spectral density close to the band edge at B . The dashed line marks the artifact which is removed by setting $\rho(\omega > \omega_{\min}) = \rho(\omega_{\min})$. The left band edge is treated accordingly.

once the subscript $_1$ is replaced by $_n$ and the subscript $_0$ by $_{n-1}$.

APPENDIX B: REMOVAL OF DECONVOLUTION ARTIFACTS

1. Outer band edges

The raw data $\{g_{ij}\}$ from D-DMRG cover only a certain finite interval. Hence the underlying unbroadened spectral density $\rho(\omega)$ can also be determined only on a finite interval $[-B, B]$ ($B \approx 3D$) which is very close to the interval in which the raw data are available. The deconvolution leads to an abrupt increase of the deconvolved $\rho(\omega)$ at the assumed band edges at B , see Fig. 23. This increase is definitely an artifact. In general, we expect that the spectral density $\rho(\omega)$ continues to decrease for $|\omega| \rightarrow \infty$. This decrease is a gradual one, i.e., there is no band edge in the strict sense for the correlated system. However, all results obtained so far by us and others²⁹ point into the direction that the contributions beyond a certain interval can be safely neglected.

The artificial increase is removed by replacing $\rho(\omega)$ for frequencies beyond ω_{\min} where the first minimum occurs by the minimal value $\rho(\omega_{\min})$. This is indicated by the dashed line in Fig. 23 which is replaced by the solid curve.

2. Inner band edges of the insulator

The situation close to inner band edges stemming from a gap is similar to the one close to outer band edges. The LB deconvolution of the D-DMRG raw data in the region, where the insulating solution displays a gap, leads to small artifacts as shown in Fig. 24 by the dashed lines.

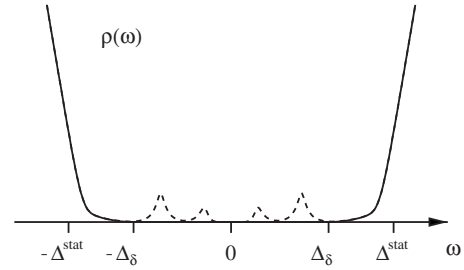


FIG. 24. Lines: generic deconvolved spectral density in the region of the gap Δ of the insulating phase. The dashed line marks the artifacts which are cut out by setting $\rho(\omega)$ to zero for $\omega \in [-\Delta_\delta, \Delta_\delta]$.

The first remedy, which one may consider, is to determine the gap Δ^{stat} of the SIAM by conventional static DMRG and to use this value as the gap of the lattice problem in DMFT. However, we found out that even an extrapolation of this static gap Δ^{stat} to the thermodynamic limit $L \rightarrow \infty$, as proposed in Ref. 27, cannot be used in our iterations. No stable self-consistent solution in the sense of the criteria given in Sec. II C 4 could be obtained.

The successful treatment of the artifacts consisted in removing only the obviously artificial features which are depicted by dashed lines in Fig. 24. The solid lines are kept because they represent real spectral weight. This is done by starting from the value of the static gap Δ^{stat} adjusted by a correction parameter $\delta > 0$

$$\rho(\omega) \equiv 0 \quad \forall \omega \in [-\Delta^{\text{stat}} + \delta, \Delta^{\text{stat}} - \delta]. \quad (\text{B1})$$

The value δ is chosen carefully, so that on the one hand all deconvolution artifacts are removed and on the other hand the proper spectral weight of the Hubbard bands stays untouched. In order to determine the appropriate value of δ it is helpful to resolve the inner Hubbard band edges in detail, which can be achieved by small values of η_i in this region. Note that the adjusted interval $[-\Delta^{\text{stat}} + \delta, \Delta^{\text{stat}} - \delta]$ can be set smaller than the interval $[-\Delta, \Delta]$ defined by the proper gap Δ as long as all deconvolution artifacts are removed. The artifacts would spoil the DMFT self-consistency iteration because the continued fraction coefficients could not be evaluated properly.

It turns out that δ does not need to be changed in each iteration of the DMFT self-consistency cycle. It is sufficient to set it once for each value of U .

*karski@uni-bonn.de

†carsten.raas@uni-dortmund.de

‡goetz.uhrig@uni-dortmund.de; URL: <http://t1.physik.uni-dortmund.de/uhrig/>

¹W. Metzner and D. Vollhardt, Phys. Rev. Lett. **62**, 324 (1989).

²E. Müller-Hartmann, Z. Phys. B: Condens. Matter **74**, 507

(1989).

³A. Georges and G. Kotliar, Phys. Rev. B **45**, 6479 (1992).

⁴M. Jarrell, Phys. Rev. Lett. **69**, 168 (1992).

⁵S. R. White, Phys. Rev. Lett. **69**, 2863 (1992).

⁶S. R. White, Phys. Rev. B **48**, 10345 (1993).

⁷S. Ramasesha, S. K. Pati, H. R. Krishna-Murthy, Z. Shuai, and J.

- L. Brédas, *Synth. Met.* **85**, 1019 (1997).
- ⁸T. D. Kühner and S. R. White, *Phys. Rev. B* **60**, 335 (1999).
- ⁹C. Raas, G. S. Uhrig, and F. B. Anders, *Phys. Rev. B* **69**, 041102(R) (2004).
- ¹⁰M. Karski, C. Raas, and G. S. Uhrig, *Phys. Rev. B* **72**, 113110 (2005).
- ¹¹J. Kanamori, *J. Phys. Chem. Solids* **10**, 87 (1959).
- ¹²J. Hubbard, *Proc. R. Soc. London, Ser. A* **276**, 238 (1963).
- ¹³M. C. Gutzwiller, *Phys. Rev. Lett.* **10**, 159 (1963).
- ¹⁴G. Kotliar, *Eur. Phys. J. B* **11**, 27 (1999).
- ¹⁵M. Karski, Diplomarbeit, Universität zu Köln, 2004; available at <http://t1.physik.uni-dortmund.de/uhrig/>
- ¹⁶M. Potthoff, *Eur. Phys. J. B* **36**, 335 (2003).
- ¹⁷G. S. Uhrig, *Phys. Rev. Lett.* **77**, 3629 (1996).
- ¹⁸A. Georges, G. Kotliar, W. Krauth, and M. J. Rozenberg, *Rev. Mod. Phys.* **68**, 13 (1996).
- ¹⁹E. N. Economou, *Green's Functions in Quantum Physics*, Solid State Sciences Vol. 7 (Springer, Berlin, 1979).
- ²⁰D. G. Pettifor and D. L. Weaire, *The Recursion Method and its Applications*, Springer Series in Solid-State Sciences Vol. 58 (D. G. Pettifor and D. L. Weaire, Berlin, 1985).
- ²¹A. C. Hewson, *The Kondo Problem to Heavy Fermions* (Cambridge University Press, Cambridge, 1993).
- ²²K. A. Hallberg, *Phys. Rev. B* **52**, R9827 (1995).
- ²³C. Raas and G. S. Uhrig, *Eur. Phys. J. B* **45**, 293 (2005).
- ²⁴T. Hövelborn, Diplomarbeit, Universität zu Köln/Universität Bonn, 2000; available at <http://t1.physik.uni-dortmund.de/uhrig/>
- ²⁵C. Raas, Ph.D. thesis, Universität zu Köln, 2005; available at <http://www.raas.de/>
- ²⁶W. H. Press, S. A. Teukolsky, W. T. Vetterling, and B. P. Flannery, *Numerical Recipes* (Cambridge University Press, Cambridge, 1992).
- ²⁷S. Nishimoto, F. Gebhard, and E. Jeckelmann, *J. Phys.: Condens. Matter* **16**, 7063 (2004).
- ²⁸S. Nishimoto, F. Gebhard, and E. Jeckelmann, *Physica B* **378-380**, 283 (2006).
- ²⁹M. P. Eastwood, F. Gebhard, E. Kalinowski, S. Nishimoto, and R. M. Noack, *Eur. Phys. J. B* **35**, 155 (2003).
- ³⁰E. Jeckelmann, *Phys. Rev. B* **66**, 045114 (2002).
- ³¹*The Recursion Method; Application to Many-Body Dynamics*, Lecture Notes in Physics Vol. m23, edited by V. S. Viswanath and G. Müller (Springer, Berlin, 1994).
- ³²F. Gebhard, E. Jeckelmann, S. Mahler, S. Nishimoto, and R. M. Noack, *Eur. Phys. J. B* **36**, 491 (2003).
- ³³D. J. García, K. Hallberg, and M. J. Rozenberg, *Phys. Rev. Lett.* **93**, 246403 (2004).
- ³⁴S. Nishimoto and E. Jeckelmann, *J. Phys.: Condens. Matter* **16**, 613 (2004).
- ³⁵N. Blümer and E. Kalinowski, *Physica B* **359**, 648 (2005).
- ³⁶N. Blümer and E. Kalinowski, *Phys. Rev. B* **71**, 195102 (2005).
- ³⁷M. J. Rozenberg, G. Kotliar, and X. Y. Zhang, *Phys. Rev. B* **49**, 10181 (1994).
- ³⁸D. E. Logan, M. P. Eastwood, and M. A. Tusch, *J. Phys.: Condens. Matter* **9**, 4211 (1997).
- ³⁹J. Hubbard, *Proc. R. Soc. London, Ser. A* **281**, 401 (1964).
- ⁴⁰R. Bulla (private communication).
- ⁴¹A. Georges and G. Kotliar, *Phys. Rev. B* **45**, 6479 (1992b).
- ⁴²M. J. Rozenberg, X. Y. Zhang, and G. Kotliar, *Phys. Rev. Lett.* **69**, 1236 (1992).
- ⁴³A. Georges and W. Krauth, *Phys. Rev. B* **48**, 7167 (1993).
- ⁴⁴M. Caffarel and W. Krauth, *Phys. Rev. Lett.* **72**, 1545 (1994).
- ⁴⁵O. Sakai and Y. Kuramoto, *Solid State Commun.* **89**, 307 (1994).
- ⁴⁶R. Bulla, *Phys. Rev. Lett.* **83**, 136 (1999).
- ⁴⁷R. Bulla, T. A. Costi, and D. Vollhardt, *Phys. Rev. B* **64**, 045103 (2001).
- ⁴⁸G. Moeller, Q. Si, G. Kotliar, M. J. Rozenberg, and D. S. Fisher, *Phys. Rev. Lett.* **74**, 2082 (1995).
- ⁴⁹O. Sakai, Y. Shimizu, and T. Kasuya, *J. Phys. Soc. Jpn.* **58**, 3666 (1989).
- ⁵⁰T. A. Costi and A. C. Hewson, *Physica B* **163**, 179 (1990).
- ⁵¹N. Blümer, Ph.D. thesis, Universität Augsburg, 2002. *ibid.* Shaker Verlag, Aachen 2003.
- ⁵²T. Pruschke, D. L. Cox, and M. Jarrell, *Phys. Rev. B* **47**, 3553 (1993).
- ⁵³E. Müller-Hartmann, *Z. Phys. B: Condens. Matter* **57**, 281 (1984).
- ⁵⁴X. Y. Zhang, M. J. Rozenberg, and G. Kotliar, *Phys. Rev. Lett.* **70**, 1666 (1993).
- ⁵⁵S. K. Kehrein, *Phys. Rev. Lett.* **81**, 3912 (1998).
- ⁵⁶R. Bulla and M. Potthoff, *Eur. Phys. J. B* **13**, 257 (2000).
- ⁵⁷P. Nozières, *Theory of Interacting Fermi Systems* (Addison-Wesley, Reading, MA, 1997).
- ⁵⁸D. J. Garcia, E. Miranda, K. Hallberg, and M. J. Rozenberg, *Phys. Rev. B* **75**, 121102(R) (2007).
- ⁵⁹Note that we use here the definition that Δ is the energy from the Fermi energy at $\omega=0$ to the lower inner band edge. This implies that the present definition is by a factor of 2 lower than the one in Ref. 32.
- ⁶⁰On the Bethe lattice there is no momentum. So, in fact, we consider a translationally invariant lattice with a semielliptic local DOS $\rho^0(\omega)$.